



2018

## DETERMINING TIDAL CHARACTERISTICS IN A RESTORED TIDAL WETLAND USING UNMANNED AERIAL VEHICLES AND DERIVED DATA

Victor Thornton  
*Virginia Commonwealth University*

Follow this and additional works at: <https://scholarscompass.vcu.edu/etd>



Part of the [Environmental Sciences Commons](#)

© The Author

---

Downloaded from

<https://scholarscompass.vcu.edu/etd/5369>

This Thesis is brought to you for free and open access by the Graduate School at VCU Scholars Compass. It has been accepted for inclusion in Theses and Dissertations by an authorized administrator of VCU Scholars Compass. For more information, please contact [libcompass@vcu.edu](mailto:libcompass@vcu.edu).

DETERMINING TIDAL CHARACTERISTICS IN A RESTORED TIDAL WETLAND USING  
UNMANNED AERIAL VEHICLES AND DERIVED DATA

A Thesis submitted in partial fulfillment of the requirements for the degree of Master of Science,  
Environmental Studies at Virginia Commonwealth University.

By

Victor L. Thornton

Bachelor of Science in Environmental Studies

Minor in Biology

Virginia Commonwealth University, 2014

Major Professor: Edward Crawford, Ph.D.

Assistant Professor, Center for Environmental Studies

Virginia Commonwealth University

Richmond, Virginia

May, 2018

## Acknowledgement

I would like to thank Dr. Edward Crawford for taking me on as a master's student, and to Dr. Rodney Dyer for his advice and direction. Thank you to Ms. Jennifer Ciminelli for introducing me to the world of GIS, and for pushing me to improve. I would like to thank the Engineering Research and Development Center, Geospatial Research Laboratory (ERDC - GRL) for their support and professionalism. In particular, I would like to thank Dr. Jean Nelson, Mr. Jarrod Edwards, and Dr. John Anderson from ERDC – GRL for their support of my work. Lastly, thank you to Mr. William Shuart for introducing me to remote sensing and guiding my research interests.

## Table of Contents

	Page
List of Tables.....	iv
List of Figures.....	v
Abstract.....	vi
Introduction.....	1
Materials and Methods.....	5
Site Description.....	5
Data Acquisition.....	5
Ground Control.....	6
Image Collection.....	7
Image Processing and Accuracy Assessment.....	7
Data Analysis.....	9
Results.....	11
Discussion.....	12
Seasonal Variation and Precipitation.....	12
Unmanned Aerial Vehicle Parameters.....	13
Water Inclusion and Time Lapse.....	14
Accuracy Assessment.....	15
Study Limitations.....	17
Implications of Research .....	18
Literature Cited.....	19
Image Processing.....	45

## List of Tables

	Page
Table 1: Equipment specifications for data acquisition, processing, and analysis.....	26
Table 2: Control points used for high tide dataset.....	27
Table 3: Control points used for low tide dataset.....	28
Table 4: Flight parameters for both high and low tide flights.....	29
Table 5: High tide accuracy assessment results with incorporated ground control (units are in meters).....	30
Table 6: High tide accuracy assessment results without ground control (units are in meters).....	31
Table 7: Low tide accuracy assessment results with incorporated ground control (units are in meters).....	32
Table 8: Low tide accuracy assessment results without ground control (units are in meters).....	33

## List of Figures

	Page
Figure 1: Study Area: Kimages Creek 37°19'36.8"N, 77°12'16.0"W.....	34
Figure 2: Examples of positioned targets and photo identifiable structures used for survey coordinates of control points in Pix4D.....	35
Figure 3: Ground control points (Yellow) and check points (Blue) used for high tide dataset....	36
Figure 4: Ground control points (Yellow) and check points (Blue) used for low tide dataset....	37
Figure 5: High tide collection on 6/7/2017. Points in red indicate flight time. Water level was collected in North American Vertical Datum 1988 feet every 15 minutes from VCU Rice Rivers Center pier gauge station. For additional information, contact the Center at: <a href="https://ricerivers.vcu.edu/">https://ricerivers.vcu.edu/</a> .....	38
Figure 6: Low tide collection on 7/26/2017. Points in red indicate flight time. Water level was collected in North American Vertical Datum 1988 feet every 15 minutes from VCU Rice Rivers Center pier gauge station. For additional information, contact the Center at: <a href="https://ricerivers.vcu.edu/">https://ricerivers.vcu.edu/</a> .....	39
Figure 7: Shoreline points used to create continuous water surface elevation, and mask showing area of elevation model removed from high and low tide.....	40
Figure 8: High tide orthophoto created with ground control points.....	41
Figure 9: Low tide orthophoto created with ground control points.....	42
Figure 10: Inset views of high tide (left) and low tide (right) .....	43
Figure 11: The extent of high tide elevation above the low tide elevation. The final output is displayed above the low tide orthophoto to depict change.....	44

## **ABSTRACT**

### **DETERMINING TIDAL CHARACTERISTICS IN A RESTORED TIDAL WETLAND USING UNMANNED AERIAL VEHICLES AND DERIVED DATA**

By Victor L. Thornton

A Thesis submitted in partial fulfillment of the requirements for the degree of Master of Science,  
Environmental Studies at Virginia Commonwealth University.

Virginia Commonwealth University, 2018

Major Professor: Edward Crawford, Ph.D.

Assistant Professor, Center for Environmental Studies

Unmanned aerial vehicle (UAV) technology was used to determine tidal extent in Kimages Creek, a restored tidal wetland located in Charles City County, Virginia. A Sensefly eBee Real-Time Kinematic UAV equipped with the Sensor Optimized for Drone Applications (SODA) camera (20-megapixel RGB sensor) was flown during a single high and low tide event in Summer 2017. Collectively, over 1,300 images were captured and processed using Pix4D. Horizontal and vertical accuracy of models created using ground control points (GCP) ranged from 0.176 m to 0.363 m. The high tide elevation model was subtracted from the low tide using

the ArcMap 10.5.1 raster calculator. The positive difference was displayed to show the portion of high tide that was above the low tide. These results show that UAVs offer numerous spatial and temporal advantages, but further research is needed to determine the best method of GCP placement in areas of similar forest structure.

***Key words:*** UAV, tidal wetland, photogrammetry, Kimages Creek, RMSE, eBee RTK, ground control, elevation

## INTRODUCTION

Remote sensing techniques have often been used in ecological research to collect information about remote locations. When applied to environmental phenomena, remote sensing can be used to map sediment erosion, analyze spatial vulnerability, classify land cover, monitor land use, and determine species composition (Jensen, 2007; Campbell and Wynne, 2011). Recent advances in satellite sensor technology, imaging techniques, and algorithms have made remote sensing an attractive platform to integrate into environmental response systems, such as wildfire and oil spill mitigation (Garcia-Garrido, et al., 2016; Miller et al., 2016), and long-term investigations of landscape change, specifically in areas sensitive to sea level rise along coastal boundaries (Rahman et al., 2011; Ariana et al., 2017). A number of studies (Brooks et al., 2004; Belal et al., 2014; Murray et al., 2017) have shown that the addition of remote sensing data can improve environmental assessments and risk mitigation at multiple spatial scales and ecosystem types. The products of these remote sensing programs have begun to integrate into regulatory agencies and academic institutions to improve the overall understanding and conceptualization of environmental issues in the 21<sup>st</sup> century; two well-known examples are the National Land Cover Database (NLCD) by U.S. Geological Survey, and the National Wetland Inventory (NWI) by U.S. Fish and Wildlife Service. Moreover, as the use of remote sensing platforms grows, the call for active sensors capable of better resolutions has given rise to an increasing number of environmental studies utilizing airborne and terrestrial Light Detection and Ranging (LiDAR) (MacDonald, 2005; Slatton et al., 2008; Ussyshkin and Theriault, 2011; Zhang K., 2011; Kulawardhana et al., 2017).

The overall expansion of remote sensing products in regulatory agencies and academic institutions has increased at a remarkable rate, making it an attractive choice for geospatial

research, and yet, remotely sensed data remains prohibitive for many researchers. For example, the difficulties associated with collecting, processing, and analyzing airborne LiDAR is a recurrent theme in ecological research (Gatziolis and Andersen, 2008; Hummel et al., 2011). Costs involving equipment, personnel, fuel, and accuracy requirements are only a few expenditures that come with LiDAR data acquisitions. Depending on the provider, additional fees may also apply (e.g. classification groups, point density, resurvey cost, etc.). With regard to satellite imagery, varying image collection periods and adverse weather conditions, such as cloud cover, can hinder multi-temporal studies by reducing the amount of available data (Weng and Weng, 2014). High spatial resolution imagery from satellites must also be purchased individually or per area, which can become costly for large scale research (Klema, 2011). Furthermore, the expertise required to use LiDAR and satellite imagery is often a constraint that must be addressed before undertaking a project of any substantial scale. Simply put, even today the application of remote sensing can be limited by the operator's skill, the various parameters and calibrations present, and the budget at hand (Jensen, 2007).

To address some of these challenges, Unmanned Aerial Vehicles (UAV) and photogrammetry have become a viable option for environmental remote sensing in recent years (Klema, 2015). UAV technology utilizes Structure from Motion (SfM), the geometric theory used in the field of photogrammetry to estimate 3-D features from a collection of static images (Ullman, 1979). To optimize SfM during the reconstruction process, the camera's position and calibration are defined for each image through a process known as the bundle adjustment. Typically, most photogrammetric software use SfM in conjunction with Multiview algorithms to improve the 3-D construction. Multiview algorithms detect homologous points within overlapping images, often referred as tie points, to triangulate positional coordinates within the

dataset. A large number of overlapping features will increase the success of the combined methodology and allow for a more accurate reconstruction (James and Robson, 2012; Riquelme et al., 2017). The final products of SfM and Multiview algorithms can include, orthometric mosaics (referred to as orthophotos moving forward), dense point clouds, and Digital Elevation Models (DEMs) of the terrain.

UAV technology offers flexibility through various frame types (fixed wing, multirotor, etc.), and customization of onboard cameras, making it an attractive method for monitoring dangerous, inaccessible, or difficult to access areas. The light weight of civilian UAVs (~1-150 kg) enables the user to conduct quick flight missions that can be repeated with minor preparation. Additionally, low-flying UAVs have the benefit of producing high spatial resolution imagery (<10 cm) (Lechner et al., 2012; Mesas-Carrascosa et al., 2016), which can be viewed immediately after the flight. Lastly, the cost of using UAVs for data acquisition is typically less expensive than conventional remote sensing techniques, given the associated costs of UAVs are generally a one-time expenditure and have potentially minor software and hardware upkeep costs.

Studies have shown that the characteristics of UAV technology are not only beneficial for ecological assessments, but ideal in rapidly changing environments like coastal wetlands (Jensen et al., 2011; Casella et al., 2016; Long et al., 2016). However, given the recent onset of autonomous aircrafts in both public and private research (Floreano and Wood, 2015; Pajares, 2015), there are relatively few studies implementing UAV and photogrammetry to extract horizontal and vertical coordinate data in coastal ecosystems. Therefore, the goal of this study was to illustrate the practicality of using UAVs in place of LiDAR and traditional remote based approaches in a rapidly changing environment. To accomplish this goal, the extent of tidal

exchange in Kimages Creek, a restored tidal wetland in Charles City County, Virginia, was investigated. The extent of tidal exchange in this region is of continued interest to the parties involved with the creek's restoration in 2010 (Virginia Commonwealth University (VCU) community partners, National Oceanic and Atmospheric Administration (NOAA), American Rivers, and The Nature Conservancy). In order to gauge the effectiveness of using UAV technology in Kimages Creek, the objective of this research was twofold: (1) determine positional accuracy of acquired data by comparing model outputs created with and without ground control points (GCP), using check points (CP) to estimate accuracy; (2) quantify the extent of a high and low tide in Kimages Creek using UAV derived data.

## **MATERIALS AND METHODS**

### **Site Description**

Kimages Creek is a tidal freshwater creek located in Charles City County, Virginia, at the VCU Rice Rivers Center (Figure 1). The portion of the creek within the Rice Rivers Center property is approximately 1800 m long and has confluence with the James River. In 1927, an earthen dam was erected at the mouth of the creek, creating the impoundment Lake Charles. The earthen dam eliminated tidal exchange between Kimages Creek and the James River, subsequently disrupting normal ecological processes characteristic of tidal wetlands for nearly eighty years. In 2006, excessive rainfall had caused the dam to breach, allowing for channelized flow to be partially restored. In 2010, VCU community partners, NOAA, American Rivers, and The Nature Conservancy removed part of the dam at the historical mouth of Kimages Creek in order to re-establish naturalized tidal flow. The removal of the dam at Kimages Creek has been considered a success, as researchers have recorded an increase in water fluxes two years following the restoration (Bukaveckas and Wood, 2014).

### **Data Acquisition**

The Sensefly (Cheseaux-Lausanne, Switzerland) eBee Real-Time Kinematic (RTK) equipped with Sensor Optimized for Drone Applications (SODA) camera were selected for image collection (Table 1). The SODA is a RGB camera with 2.9 cm/pixel ground resolution when flown at 122 m, and a sensor size of 12.75 x 8.5 mm. The eBee RTK UAV provides survey grade accuracy with the use of a virtual or physical base station and is able to cover 12 km<sup>2</sup> in a single flight. If used with a base station, the built in Global Navigation Satellite System (GNSS)

in the eBee RTK receives corrections from the base station and appends the geographic information to each image for post-processing in eMotion, Sensefly's flight planning software.

For this study, the base station Topcon HiPER V<sup>®</sup> (Livermore, CA) was used in combination with a known position captured with a Trimble NetR9 GNSS Reference Receiver (Sunnyvale, CA) over a six-hour logging period. The logging period resulted in a raw satellite navigation file with a Root Mean Square Error (RMSE) of 0.013 m, which was submitted to NOAA's Online User Positioning Service (OPUS) to extract point location (NOAA, 2017). The coordinates were then entered into the base station which was set on a 2 m tripod. This point was then broadcasted to the eBee RTK for corrections via eMotion3. Pix4D<sup>®</sup> (Lausanne, Switzerland) was used for model creation, and ground control processing. Lastly, ESRI's ArcMap 10.5.1 (Redlands, CA) was used for final dataset analysis.

## **Ground Control**

The U.S. Army Corps of Engineers (USACE) Vertical Accuracy Standards recommend that a study site  $\leq 500 \text{ km}^2$  in area have twenty static CP in order to properly assess the accuracy of geometrically corrected aerial images (also known as orthophotos) and elevation datasets created from LiDAR and stereo photogrammetry (U.S. Army Corps of Engineers, 2015). Given the size of Kimages Creek ( $\sim 0.214 \text{ km}^2$ ), we decided that a total of eleven well distributed control points would be sufficient for a collection of this size (Table 2 and Table 3). A combination of artificial targets and photo identifiable structures (e.g. pavement tiles and corner of buildings) were used as markers for all control points (Figure 2). The Trimble NetR9 GNSS Reference Receiver logged the position of these markers to collect all control points throughout the study area using the same base station coordinates procedure with an average logging time of

three hours. Six of the control points were used as GCPs to georeference the imagery, and five of the control points were used as CPs to assess accuracy of the high and low tide datasets (Figures 3 and 4, respectively). The average RMSE of these points was 0.165 m. This averaged error is omitting the following three points which had missing OPUS solutions: (1) the most northern point used as GCP 6 in the low tide dataset, (2) the southern point near the mouth of Kimages creek used as GCP 4, and (3) the southern point used as CP 4.

## **Image Collection**

Intertidal zones along the east coast of North America experience semidiurnal tides, two high and two low tides over one twenty-four-hour period. Image collection began when high and low tide coincided with high sun angle, as standing trees in forested areas can reduce the amount of available light in photographs. Without adequate illumination, images are prone to dark or missing cells due to shadows (Mesas-Carrascosa et al., 2016). Ideally, high and low tide collections would have been on the same day, however given logistical constraints, the flights were separated between 6/7/2017 and 7/26/2017 (Figures 5 and 6). High tide on 6/7/2017 was at approximately 14:51 hrs. (solar elevation  $63.59^{\circ}$ , solar azimuth at  $243.34^{\circ}$ ) and flights began at 15:30 hrs. Low tide on 7/26/2017 was at approximately 12:47 hrs. (solar elevation  $70.63^{\circ}$ , solar azimuth at  $158.7^{\circ}$ ) and flights began at 13:00 hrs. (NOAA, 2017) (Table 4). Both days had relatively low winds and cloud cover, proving adequate field conditions for flight.

## **Image Processing and Accuracy Assessment**

Pix4D was used to process aerial imagery and conduct the accuracy assessment for all datasets. Pix4D's ray cloud editor was used to improve the construction of the GCP-incorporated models by manually adding two and seven manual tie points to the high and low tide processing,

respectively. These additional manual tie points can reduce missing data and gaps within the orthophotos by increasing the number of photographs included during processing. Manual tie points are used by Pix4D in the same way as automatic tie points, the main difference being that they are chosen by the user instead of the software. The process of choosing manual tie points requires the user to look through overlapping calibrated photographs to find homologous points (e.g. the corner of highly reflective material). Once these points are found the user must then establish them as a manual tie point via the ray cloud editor. In Pix4D, each photograph is required to have at least twenty tie points (can be any combination of manual/automatic tie points) to be used in the reconstruction process.

Horizontal and vertical coordinates of all datasets were validated using a Root Mean Square Error (RMSE) approach. In photogrammetry, this is often used to estimate error between the observed map values within an orthophoto and the reference sample locations (Check Points) within the dataset (Congalton and Green, 2009; Fischer et al., 2017, technical report submitted for publication). Pix4D was used to generate the RMSE, mean error, and sigma (the standard deviation of each CP). The following formulas are how Pix4D defines RMSE, mean error, and sigma, where  $n$  is the total number of GCPs, and  $e_i$  is the error of each point for the given direction.

$$(1) \text{ RMSE} = \sqrt{(\sum(e_i^2)/n)}$$

$$(2) \text{ Mean error} = \mu = \sum(e_i)/n$$

$$(3) \text{ Sigma} = \sigma = \sqrt{(\sum(e_i - \mu)^2/n)}$$

## **Data Analysis**

Images were geotagged in World Geodetic System 1984 (WGS 84) and later transformed into the North American Datum 1983 (NAD 1983), and the North American Vertical Datum 1988 (NAVD 88) for analysis. Using ESRI's ArcMap 10.5.1 spatial analysis toolbox, the boundary of Kimages Creek was clipped from the final orthophotos with the HUC 8 Watershed Boundary shapefile (USFWS, 2017).

In order to address uncertainty in the elevation models, the point clouds created from the GCP-incorporated analysis went through geostatistical simulations using the ArcMap 10.5.1 spatial analysis and 3-D analysis toolboxes. The Pix4D point clouds for high and low tide were first converted to a point shapefile containing the elevation values. The average point spacing for each point cloud to shapefile conversion was based on the ground sampling distance reported by the GCP-incorporated Pix4D output (0.0316 m and 0.0308 m for high and low tide, respectively). A prediction surface type simple kriging layer was then created from those points using a normal score transformation to maintain a normal distribution of points within the Kimages Creek boundary. The resulting simple kriging layer was then used as the input for the Gaussian Geostatistical Simulations (GGS) tool to create ten raster simulations. The conditional error input for each simulation was based on the RMSE of the elevation, which was obtained from the Pix4D CP analysis. The simulations were summarized as a single averaged elevation raster (0.10 m pixel size) for both low and high tide. The floating-point elevation values for both elevation rasters were then rounded up to the nearest 100<sup>th</sup> place.

Large elevation spikes and valleys found in the mid to lower regions within the water channel. These abrupt elevation changes were mostly found in water-only sections of the data, as

the reconstruction process struggles with water inclusion. In order to deal with these unreliable values, one continuous water surface elevation was given for the channel in both high and low tide datasets. To accomplish this in ArcMap 10.5.1, seven hundred shapefile points were created along the shoreline of the gaussian elevation rasters and then averaged to obtain a continuous water surface elevation value of 0.885 m and 0.538 m for the high and low tide, respectively (Figure 7). Using the extract by mask tool, all original cell values within the boundary of these points were erased, and then replaced with the above elevation values via the raster calculator. Lastly, the high and low tide gaussian elevation rasters were compared using the raster calculator to quantify the difference in elevation between both datasets. The high tide was subtracted from the low tide, and then all negative values in the resulting output were removed to show only the elevation of the high tide that was above the low tide.

## RESULTS

The high and low tide acquisitions were processed with and without ground control resulting in four datasets. The Pix4D quality reports indicated that for all datasets, 55% and 47% of the total images were used for model creation from high and low tide flights, respectively. Despite losing photos during the meshing process, the high and low tide orthophoto products comprised all of Kimages Creek at high tide (Figure 8) and low tide (Figure 9). Visual differences between the high and low tide orthophotos are displayed in sections (Figure 10). The subtraction of the high tide elevation model from the low tide elevation model resulted in the total difference in elevation from high tide (6/7/2017) to low tide (7/26/2017). The removal of all negative values from the resulting output illustrates the amount and extent in which high tide was above the low tide. (Figure 11).

The high tide dataset created with GCPs had a RMSE of 0.343 m (RMSE<sub>x</sub>), 0.252 m (RMSE<sub>y</sub>), and 0.232 m (RMSE<sub>z</sub>) (Table 5). The high tide dataset created without GCPs had a RMSE of 0.358 m (RMSE<sub>x</sub>), 0.130 m (RMSE<sub>y</sub>), and 1.765 m (RMSE<sub>z</sub>) (Table 6). The low tide analysis produced similar results. The low tide dataset created with GCPs had a RMSE of 0.383 m (RMSE<sub>x</sub>), 0.176 m (RMSE<sub>y</sub>), and 0.363 m (RMSE<sub>z</sub>) (Table 7). The low tide dataset created without GCPs had a RMSE of 0.367 m (RMSE<sub>x</sub>), 0.370 m (RMSE<sub>y</sub>), and 0.480 m (RMSE<sub>z</sub>) (Table 8). These results indicate that using GCPs in the workflow enhanced the accuracy of some positional coordinates, while having minimal affect in others. In addition, CP 3 is absent in the low tide analysis because this marker's position was lost after it was driven over by cars following the earlier high tide collection.

## **DISCUSSION**

This study employed emerging techniques to illustrate the practicality of using UAVs to evaluate change in tidal wetlands. The photo meshing process had very few issues aligning photographs that comprised only Kimages Creek to create orthophotos. However, some errors did occur while matching photos in the dense forest areas surrounding the creek margins, which resulted in gaps and distorted sections in the final models. In addition, photos that comprised mostly trees were dropped out of the orthophoto creation process. The generated 3-D point cloud also suffered slightly from outliers and missing data in the dense forest areas and water sections within the channel. Slight discrepancies were also found between high and low tide orthophotos due to external factors such as cloud cover and sun angle. For example, the low tide collection benefited from a higher sun elevation ( $\sim 10^\circ$  higher) during image acquisition, which resulted in a brighter orthophoto. This improved visibility and overall representation of the study area during low tide. The final high and low tide elevation comparison illuminates the extent of high tide that is above the low tide. The results of this study have demonstrated the feasibility of using UAVs in place of LiDAR and traditional remote based approaches to capture horizontal and vertical coordinate data in rapidly changing environments. To understand the change found in the derived data, seasonal variation, precipitation, UAV parameters, water inclusion, time lapses, and data accuracy were further considered.

### **Seasonal Variation and Precipitation**

Water movement in tidal wetlands is dependent on numerous factors such as, vegetation abundance, available precipitation, and the position of the sun and moon (Fretwell et al., 1996). Our two usable flights were collected on 6/7/2017 and 7/26/2017, and thus, variations in these

factors were inconsistent between both datasets. For example, while both collection dates were within the summer of 2017, the forty-nine-day difference between them presents a discrepancy in the amount of time vegetation had opportunity to grow. Originally, this variation was to be avoided by collecting each tide immediately after the other, but external forces (day light availability, weather conditions, UAV malfunctions, etc.) made this unfeasible. In addition, precipitation rates prior to the high tide flight (6/7/2017) were higher than the low tide flight (7/26/2017). In Charles City County, VA, 6/5/2017 and 6/6/2017 experienced ~0.50-0.75 in of total rainfall, while 7/24/2017 and 7/25/2017 had no rain, and 7/23/2017 had extremely light showers (~0.10 in) throughout the day (NOAA, 2017). Lastly, the moon phase of the high tide flight was waxing gibbous, two days before a full moon, while the moon phase of the low tide flight was waxing crescent, three days after a new moon (NOAA, 2018). To varying degrees all of these factors likely influenced the amount of visible water seen in both orthophotos.

### **Unmanned Aerial Vehicle Parameters**

The parameter settings for the UAV were most notably influenced by the size of Kimages Creek, the height of surrounding trees (~30-40 m), and the required spatial resolution. One of the most challenging parameters to set was the UAV's distance above ground level (AGL). Setting a low AGL will produce images that have a high spatial resolution but increase the amount of battery replacements and overall flight duration. Conversely, increasing the AGL will reduce the flight time, insuring atmospheric properties remain relatively constant (i.e., sun angle, cloud cover, wind speed), but at the risk of lowering spatial resolution. For this study, we decided that 122 m AGL was the best possible agreement between these factors. The Sensefly SODA (2.9 cm/pixel ground resolution) enabled us to fly the eBee RTK at 122 m AGL and receive images with enough resolution to see fine details within our area of interest. Using a camera of high

spatial resolution was beneficial to the second objective of this study, which was to quantify the extent of tidal influence within the creek over one low and high tidal event.

The image reconstruction technique used in this study was hindered by the abundance of trees surrounding Kimages Creek. Some studies have shown the limitation of the photogrammetry process in complex forest environments due to factors such as, shadows, canopy occlusion, and irregular tree crown shape (Jarnstedt et al., 2012; Wallace et al., 2016; Mohan et al., 2017; White et al., 2018). While there are few trees within Kimages creek itself, the surrounding forest included in our flight plan did reduce the number of photographs useable during photo-reconstruction. The final models were created using only 55% and 47% of the total images collected for high and low tide, respectively. The majority of the unused images in both datasets comprised canopy-only features. In addition, we believe the elevation difference between tree canopy and the wetland presented an issue with the bundle block adjustment during autocorrelation. The camera in this study was set to auto-focus its lens depending on what was directly below it. Since the difference in elevation between tree canopy and the wetland was in many cases  $\geq 30$  m, numerous photos became unusable, or ‘fell-out’ of processing. However, as the resulting clipped orthophotos indicate, if only the wetland itself is flown the data comes out with fewer gaps and stitching errors in the orthophotos. This is likely because the elevation of the wetland has less drastic elevation changes compared to a collection that incorporates both the wetland and the surrounding forest.

### **Water Inclusion and Time Lapse**

In addition to the difficulties of capturing trees, the inclusion of water was another variable that reduced data quality. The featureless, reflective, and constant motion of water in

this study made model construction difficult during the photogrammetric process and required a continuous water surface elevation to be calculated using elevation values averaged from the shoreline. The orthophotos did turn out well enough to make visual comparisons, but because of inconsistent sun angles between flights, there was a disproportionate amount of light reflection in the water sections. This variation limited orthophoto comparisons to visual-only, as subtracting the orthophotos would show us unwanted pixel difference between high and low tide.

While the orthophoto comparisons show discernable difference between the high and low tide, it should be noted that the final products of these flights are stitched together photos taken at different points in time. The peak high and peak low of the tides lasted only for a few minutes, after which point the water level changed (Figures 5 and 6, respectively). In addition, there is a lag time between the water level at the southern and northern regions of the creek. For this study, we decided the best time to fly would be at the estimated peak of the respective high and low tides. For other studies, the optimal time to fly would depend on what portion of the creek is under investigation. By tailoring the UAV launch time in this way, the output would depict a more holistic representation of the tidal event in the specific area of interest.

### **Accuracy Assessment**

As shown from the results of this study, the datasets processed with ground control turned out to be more accurate than datasets processed using only the onboard accuracy of the eBee RTK. In general, the benefit of using the eBee RTK is that the built in GNSS receiver make GCPs unnecessary. This feature can be attractive to researchers that do not have the time, budget, or equipment to capture ground control over a large collection area. An accuracy assessment was performed by Sensefly technicians to confirm the survey grade accuracy of the eBee RTK (Rose

et al., 2017). (Rose et al., 2017) flew the eBee RTK over a 0.20 km<sup>2</sup> area in both optimal and adverse weather conditions. The result from their assessment indicated that without GCP, the eBee RTK was able to achieve accuracy within one to three times the ground sampling distance. Additionally, (Rose et al., 2017) demonstrated that by manually editing 10% of their total images with incorrect geotags, the eBee RTK was still able to produce between 0.028 m and 0.048 m RMSE in horizontal and vertical coordinates, respectively.

Our results showed slightly higher RMSE using the eBee RTK in Kimages Creek, a study site of similar size (~0.214 km<sup>2</sup>). Accuracy results indicate that without GCP, horizontal and vertical coordinates RMSE ranged around 0.130 m to 1.765 m. Although the addition of GCP in the photogrammetric process did improve this error in some cases, it is possible that many of the images captured in our flights suffered from a large number of incorrect geotags (>10%). Kimages Creek is a complex area of study because of its length and the abundance of standing vegetation, and thus, we suspect that the distance the eBee RTK needed to travel combined with the high standing vegetation, limited the data-link connection of the eBee RTK and base station. This weakened connection possibly resulted in less image corrections during the flight and reduced the accuracy of the geotagged images. In addition, the quality of our GCP and CP was also likely a factor that reduced model accuracy. Opportunities for GCP placement were extremely limited in this study area due to high standing vegetation and lack of solid ground within the wetland. The GCP-incorporated quality reports from Pix4D indicated that for both high and low tide, our GCP error was two times greater than the ground sampling distance which caused degradation in the model accuracy detailed in the accuracy assessment. It is extremely likely that the poor accuracy of some of our GCPs and CPs was due to their placement in forested areas that had large amounts of obtrusive canopy. These result indicate other alternatives

for control point placement in wetlands must be explored if positional error is to be reduced in similar study areas. Overall, these factors made it necessary to address the uncertainty in our data by using the GGS tool during data analysis.

## **Study Limitations**

The most notable limitation of this study was processing a full image scene of Kimages Creek. Open Drone Map was originally used for this study because the benefits of open-sourced software—flexibility, low cost, community collaboration—are aspects not easily found in commercial software. Unfortunately, due to the size of Kimages Creek, the surrounding forest hindering the meshing process, and potentially other unexplored reasons, Open Drone Map was unable to process a large portion of photos in the dense forested regions. Thus, many GCP and CP around the edges of the flight area were lost. Pix4D was then employed for GCP processing and model creation because of the included ray cloud editor. While it is unclear how well the addition of manual tie points improved the image processing specifically, using Pix4D did allow for all original GCP and CP to be implemented into the analysis. The only exception was CP 3 in the low tide dataset, which was not visible in any photographs from the low tide collection and thus omitted from analysis. Furthermore, the number of images collected, the time it took to complete a flight, and even the amount of batteries available for the UAV, were all contingencies that required constant attention. On multiple occasions, poor weather conditions (high winds, low sun angle, cloud cover) made the decision to fly nebulous or otherwise impossible. Lastly, the high spatial resolution of our data along with the size of Kimages Creek, required a significant amount of computer resources and processing time. The amount of simulations run and output cell size with the GGS tool, for example, were limited by the amount of available computer resources (our work stations contained a NVIDIA Quadro K5200 8 GB graphics card

and 32 GB of RAM). Ten simulations with 0.10 m pixel size was the best combination of input parameters our work stations could manage. If we added more simulations or reduced the output pixel size, the process resulted in an “Out of Memory” error. Total processing time using Pix4D and the GGS tool combined was around 50-60 hours for each dataset.

## **Implications of Research**

Few studies implementing the above methodology to research vulnerable coastal ecosystems. The information gathered from this study will provide researchers a new perspective on the benefits of leveraging UAV technology in tidal wetlands. This study demonstrated that high spatial resolution can be combined with flexible collection times to obtain usable horizontal and vertical coordinate data in rapidly changing environments. Kimages Creek has significance to VCU researchers, government agencies, and advocacy groups that have put priceless time and effort into its restoration. This research builds upon a growing repository of information that will be used for the betterment of not only Kimages Creek but threatened wetlands as a collective. The next challenge that must be addressed is how to implement these high spatial resolution datasets into infrastructures that have data which is much coarser in comparison. In addition, further research is needed to determine best practices for ground control collection in non-urban areas where placement is limited by tree canopy, and flight parameters, such as UAV altitude, and the amount of necessary photo overlap for study areas of complex vegetation.

## LITERATURE CITED

- Ariana, D., Kusmana, C., and Setiawan, Y. (2017). Study Of Sea Level Rise Using Satellite Atimetry Data In The Sea Of Dumai, Riau, Indonesia. *Geoplanning: Journal of Geomatics and Planning*. 4(1), pp. 75-82.
- Belal, A., El-Ramady, H.R., Mohamed, E.S., and Saleh, A.M. (2014). Drought Risk Assessment Using Remote Sensing And GIS Techniques. *Arabian Journal of Geosciences*. 7(1), pp. 35-53.
- Brooks, R.P., Wardrop, D.H., and Bishop, J.A. (2004). Assessing Wetland Condition On A Watershed Basis In The Mid-Atlantic Region Using Synoptic Land-Cover Maps. *Environmental Monitoring and Assessment* 94(1), pp. 9-22.
- Bukaveckas, P., and Wood, J. (2014). Nitrogen Retention In A Restored Tidal Stream (Kimages Creek, VA) Assessed by Mass Balance and Tracer Approaches. *Journal of Environmental Quality*. 43(5), pp. 1614-1623.
- Campbell, J.B., and Wynne, R.H. (2011). Introduction To Remote Sensing. New York, NY: *The Guilford Press*. pp. 667.
- Casella, E., Rovere, A., Pedroncini, A., Stark, C.P., Casella, M., Ferrari, M., and Firpo, M. (2016). Drones As Tools For Monitoring Beach Topography Changes In The Ligurian Sea (NW Mediterranean). *Geo-Marine Letters*. 36(2), pp. 151-163.
- Congalton, R.G., and Green, K. (2009). Assessing The Accuracy Of Remotely Sensed Data. Boca Raton, FL: *Taylor & Francis Group*. pp. 183.
- ESRI. Company website. Accessed on 12/18/2017. Retrieved from <  
<http://www.esri.com/arcgis/about-arcgis>>.

- Fischer, R.L., Ruby, J.G., Armstrong, A.J., Edwards, J.D., Spore, N.J., and Brodie, K.L. (2017). Geospatial Accuracy Of Small Unmanned Airborne System Data In The Coastal Environment. Report no. ERDC SR-17-DRAFT, *Geospatial Research Laboratory U.S. Army Engineer Research and Development Center*, Alexandria, VA. Technical Report submitted for publication.
- Floreano, D., and Wood, R.J. (2015). Science, Technology And The Future Of Small Autonomous Drones. *Nature*. 521(7553), pp. 460-466.
- Fretwell, J.D., Williams, J.S., and Redman, P.J. (1996). National Water Summary On Wetland Resources. Report no. 2425. *United States Geologic Survey*, Washington, D.C.
- Garcia-Garrido, V.J., Ramos, A., Mancho, A.M., Coca, J., and Wiggins, S. (2016). A Dynamical Systems Perspective For A Real-Time Response To A Marine Oil Spill. *Marine Pollution Bulletin*. 112(1-2), pp. 201-210.
- Gatziolis, D., Andersen, H.E., (2008). A Guide To LIDAR Data Acquisition And Processing For The Forest Of The Pacific Northwest. Report no. PNW-GTR-768, *United States Department of Agriculture*, Pacific Northwest Research Station.
- Hummel, S., Hudak, A.T., Uebler, E.H., Falkowski, M.J., Megown, K.A. (2011). A Comparison of Accuracy And Cost Of LiDAR Versus Stand Exam Data For Landscape Management On The Malheur National Forest. *Journal of Forestry*. 109(5), pp. 267-273.
- James, M.R., and Robson S. (2012). Straightforward Reconstruction Of 3D Surfaces And Topography With A Camera: Accuracy And Geoscience Application. *Journal of Geophysical Research*. 117(F3), pp. 1-17.

- Jarnstedt, J., Pekkarinen, A., Tuominen, S., Ginzler, C., Holopainen, M., Viitala, R. (2012). Forest Variable Estimation Using A High-Resolution Digital Surface Model. *Journal of Photogrammetry and Remote Sensing*. 74, pp. 78-84.
- Jensen, A., Hardy, T., McKee, M., and Chen, Y. (2011). Using A Multispectral Autonomous Unmanned Aerial Remote Sensing Platform (AggieAir) For Riparian And Wetlands Applications. *IEEE International Geoscience and Remote Sensing Symposium*, Vancouver, BC, pp. 3413-3416.
- Jensen, J.R. (2007). Remote Sensing Of The Environment: An Earth Resource Perspective. Upper Saddle River, NJ: *Prentice Hall*. pp. 592.
- Klemas, V. (2011). Remote Sensing of Wetlands: Case Studies Comparing Practical Techniques. *Journal of Coastal Research*. 27(3), pp. 418-427.
- Klemas, V. (2015). Coastal and Environmental Remote Sensing From Unmanned Aerial Vehicles: An overview. *Journal of Coastal Research*. 31(5), pp. 1260–1267.
- Kulawardhana, R.W., Popescu, S.C., and Feagin, R.A. (2017). Airborne Lidar Remote Sensing Applications in Non-Forested Short Stature Environments: A Review. *Annals of Forest Research*. 60(1), pp. 173-196.
- Lechner, A.M., Fletcher, A., Johansen, K., and Erskine, P. (2012). Characterizing Upland Swamps Using Object-based Classification Methods And Hyper-spatial Resolution Imagery Derived From An Unmanned Aerial Vehicle. *Remote Sensing and Spatial Information Sciences*. 1-4, pp. 101-106.
- Long, N., Millescamp B., Guillot B., Pouget F., and Bertin X. (2016). Monitoring The Topography Of A Dynamic Tidal Inlet Using UAV Imagery. *Remote Sensing*. 8(5), pp. 387-402.

- MacDonald, A. (2005). New Developments Increase Use Of Airborne LIDAR Bathymetry. *Sea Technology*. 46(9), pp. 46-48.
- Mohan, M., Silva, C.A., Klauberg, C., Jat, P., Catts, Glenn., Cardil, A., Hudak, A.T., and Dia, M. (2017). Individual Tree Detection From Unmanned Aerial Vehicle (UAV) Derived Canopy Height Model In An Open Canopy Mixed Conifer Forest. *Forests*. 8(9). pp. 1-17.
- Mesas-Carrascosa, F.J., Notario-Garcia, M.D., de Larriva, J.E.M., and Garcia-Ferrer, A. (2016). An Analysis Of The Influence Of Flight Parameters In The Generation of Unmanned Aerial Vehicle (UAV) Orthomosaicks to Survey Archaeological Areas. *Sensors*. 16(11), pp. 1838.
- Miller, M.E., Elliot, W.J., Billmire, M., Robichaud, P.R., and Endsley, K.A. (2016). Rapid-Response Tools and Datasets For Post-Fire Remediation: Linking Remote Sensing And Process-Based Hydrological Models. *International Journal of Wildlife Fire*. 25, pp. 1061-1073.
- Murray, N.J., Keith, D.A., Bland, L.M., Ferrari, R., Lyons, M.B., Lucas, R., Pettorelli, N., and Nicholson, E. (2017). The Role of Satellite Remote Sensing In Structured Ecosystem Risk Assessments. *Science of the Total Environment*. 619-620, pp. 249-257.
- National Oceanic and Atmospheric Administration. Online Positioning User Service. Accessed on 9/10/2017. Retrieved from < <https://www.ngs.noaa.gov/OPUS/>>.
- National Oceanic and Atmospheric Administration. Solar Position Calculator. Accessed on 2/3/2017. Retrieved from <<https://www.esrl.noaa.gov/gmd/grad/solcalc/azel.html>>.
- National Oceanic and Atmospheric Administration. National Weather Service. Accessed on 9/26/2017. Retrieved from < <http://water.weather.gov/precip/index.php#>>.

- National Oceanic and Atmospheric Administration. Tides and Currents. Accessed on 4/28/2018.  
Retrieved from <<https://tidesandcurrents.noaa.gov/astronomical.html>>.
- Pajares, G. (2015). Overview And Current Status Of Remote Sensing Applications Based On Unmanned Aerial Vehicles (UAVs). *Photogrammetric Engineering and Remote Sensing*. 81(4), pp. 281-330.
- Pix4D. Company website. Accessed on 4/8/2018. Retrieved from <<https://pix4d.com/>>.
- Rahman, A.F., Dragoni, D., and El-Masri, B. (2011). Response Of The Sundarbans Coastline to Sea Level Rise And Decrease Sediment Flow: A Remote Sensing Assessment. *Remote Sensing of Environment*. 115(12), pp. 3121-3128.
- Riquelme, A., Cano, M., Tomas, R., and Abellan, A. (2017). Identification Of Rock Slope Discontinuity Sets From Laser Scanner And Photogrammetric Point Clouds: A Comparative Analysis. *Procedia Engineering*. 191. pp. 838-845.
- Rose, A., Zufferey, J.C., Beyeler, A., and McClellan, A. eBee RTK Accuracy Assessment. Accessed 9/24/2017. Retrieved from <[https://www.sensefly.com/app/uploads/2017/11/eBee\\_RTK\\_Accuracy\\_Assessment.pdf](https://www.sensefly.com/app/uploads/2017/11/eBee_RTK_Accuracy_Assessment.pdf)>.
- Sensefly. Company website. Accessed on 12/18/2017. Retrieved from <<https://www.sensefly.com/home.html>>.
- Slatton, K.C., Crawford M.M., and Chang L. (2008). Modeling Temporal Variations In Multipolarized Radar Scattering From Intertidal Coastal Wetlands. *Photogrammetry & Remote Sensing*. 63(5), pp. 559-577.
- Topcon. HiPER V GNSS Receiver Brochure. Accessed on 12/18/2017. Retrieved from <[https://www.topconpositioning.com/sites/default/files/product\\_files/hiper\\_v\\_broch\\_7010\\_2121\\_reve\\_sm.pdf](https://www.topconpositioning.com/sites/default/files/product_files/hiper_v_broch_7010_2121_reve_sm.pdf)>.

- Trimble. Trimble Net R9 GNSS Reference Receiver User Guide. Accessed on 12/18/2017  
Retrieved from <  
[https://geotronics.com.pl/produkty/Infrastruktura/NetR9/NetR9\\_UserGuide\\_13506.pdf](https://geotronics.com.pl/produkty/Infrastruktura/NetR9/NetR9_UserGuide_13506.pdf)>.
- Ullman, S. (1979). The Interpretation Of Structure From Motion. *The Proceedings of the Royal Society B. Biological Sciences*. 203 (1153), pp. 405-426.
- U.S. Army Corps of Engineers (2015). Photogrammetric And LiDAR Mapping. *Engineering and Design*. Accessed on 10/12/2017. Retrieved from  
<[http://www.publications.usace.army.mil/Portals/76/Publications/EngineerManuals/EM\\_1110-1-1000.pdf?ver=2016-03-25-080019-613](http://www.publications.usace.army.mil/Portals/76/Publications/EngineerManuals/EM_1110-1-1000.pdf?ver=2016-03-25-080019-613)>.
- U.S. Fish and Wildlife Service. National Wetlands Inventory HUC 8 Watershed Boundary.  
Accessed on 12/18/2017. Retrieved from <  
<https://www.fws.gov/wetlands/Data/Mapper.html>>.
- Ussyshkin, V., and Theriault, L. (2011). Airborne Lidar: Advances In Discrete Return  
Technology For 3D Vegetation Mapping. *Remote Sensing*. 3(3), pp. 416-434.
- Virginia Commonwealth University Rice Rivers Center. Accessed on 8/21/2017. Retrieved from  
<<https://ricerivers.vcu.edu/>>.
- Wallace, L., Lucieer, A., Malenovsky, Z., Turner, D., Vopenka, P. (2016). Assessment Of Forest  
Structure Using Two UAV Techniques: A Comparison Of Airborne Laser Scanning And  
Structure From Motion (SfM) Point Clouds. *Forest*. 7(3), pp. 1-16.
- Weng, J., and Weng, Q. (2014). Scale Issues In Remote Sensing. Accessed on 4/27/2018.  
Retrieved from <<https://ebookcentral-proquest-com.proxy.library.vcu.edu>>.

- White, J.C., Tompalski, P., Coops, N.C., Wulder, M.A. (2018). Comparison Of Airborne Laser Scanning And Digital Stereo Imagery For Characterizing Forest Canopy Gaps In Coastal Temperate Rainforests. *Remote Sensing of Environment*. 208, pp. 1-14.
- Zhang, K. (2011). Analysis Of Non-linear Inundation From Sea-level Rise Using LIDAR Data: A Case Study For South Florida. *Climatic Change*. 106(4), pp. 537-565.

Table 1. Equipment specifications for data acquisition, processing, and analysis.

System Weight.....	0.70 kg (~1.61 lbs.)
Wingspan.....	96 cm (38 in.)
Maximum Flight Time.....	40 min
Antenna.....	2.4 GHz radio link
Radio Range.....	3 km (~1.86 miles)
Max Wind Usage.....	45 km/h (28 mph)
Camera.....	Sensefly SODA
Base Station.....	Topcon Hyper V
Software planning.....	eMotion3
Image processing.....	OpenDroneMap and Pix4D
Image analysis.....	ArcMap 10.5.1

Table 2. Control points used for high tide dataset.

<b>POINT NAME</b>	<b>NAD83_EASTING (X)</b>	<b>NAD83_NORTHING (Y)</b>	<b>NAVD88_Height</b>
GCP 1	304458.422	4134360.936	1.430
GCP 2	304246.674	4134327.039	1.094
GCP 3	304825.340	4133489.241	2.384
GCP 4	304655.170	4133404.547	2.492
GCP 5	304395.058	4133945.225	13.661
GCP 6	304595.517	4133308.584	13.173
CP 1	304560.153	4134541.891	1.246
CP 2	304350.311	4134361.169	0.668
CP 3	304076.897	4134420.440	14.299
CP 4	304558.912	4133292.521	12.834
CP 5	304572.911	4133284.003	12.880

Table 3. Control points used for low tide dataset.

<b>POINT NAME</b>	<b>NAD83_EASTING (X)</b>	<b>NAD83_NORTHING (Y)</b>	<b>NAVD88_Height</b>
GCP 1	304458.422	4134360.936	1.430
GCP 2	304570.650	4134713.411	4.039
GCP 3	304825.340	4133489.241	2.384
GCP 4	304655.170	4133404.547	2.492
GCP 5	304395.058	4133945.225	13.661
GCP 6	304595.517	4133308.584	13.173
CP 1	304560.153	4134541.891	1.246
CP 2	304350.311	4134361.169	0.668
CP 3	304076.897	4134420.440	14.299
CP 4	304558.912	4133292.521	12.834
CP 5	304572.911	4133284.003	12.880

Table 4. Flight parameters for both high and low tide flights.

<b>Date</b>	<b>Estimated Flight Time</b>	<b>Solar Elevation</b>	<b>Solar Azimuth</b>	<b>Side/Forward Overlap</b>	<b>F stop</b>	<b>AGL</b>	<b>Image #</b>
6/7/2017	15:30 – 17:30	63.59°	243.34°	70%/70%	F/2.8	122 m	627
7/26/2017	13:00 – 14:45	70.63°	158.7°	70%/70%	F/2.8	122 m	683

Table 5. High tide accuracy assessment results with incorporated ground control (units are in meters).

<b>Point ID</b>	<b>Error X</b>	<b>Error Y</b>	<b>Error Z</b>
Checkpoint 1	-0.541	-0.311	-0.329
Checkpoint 2	0.306	-0.049	0.297
Checkpoint 3	-0.410	-0.208	0.182
Checkpoint 4	0.072	-0.410	0.032
Checkpoint 5	0.172	-0.082	-0.198
<b>Mean Error</b>	-0.080	-0.212	-0.003
<b>Sigma</b>	0.334	0.136	0.232
<b>RMSE</b>	0.343	0.252	0.232

Table 6. High tide accuracy assessment results without ground control (units are in meters).

<b>Point ID</b>	<b>Error X</b>	<b>Error Y</b>	<b>Error Z</b>
Checkpoint 1	0.354	-0.101	1.606
Checkpoint 2	0.672	0.135	1.594
Checkpoint 3	-0.010	-0.085	1.944
Checkpoint 4	-0.119	-0.219	1.958
Checkpoint 5	0.219	-0.035	1.685
<b>Mean Error</b>	0.223	-0.061	1.757
<b>Sigma</b>	0.279	0.115	0.161
<b>RMSE</b>	0.358	0.130	1.765

Table 7. Low tide accuracy assessment results with incorporated ground control (units are in meters).

<b>Point ID</b>	<b>Error X</b>	<b>Error Y</b>	<b>Error Z</b>
Checkpoint 1	0.713	0.309	0.250
Checkpoint 2	-0.130	-0.117	0.334
Checkpoint 4	0.076	0.022	-0.338
Checkpoint 5	0.233	-0.117	-0.488
<b>Mean Error</b>	0.223	0.083	-0.060
<b>Sigma</b>	0.311	0.155	0.358
<b>RMSE</b>	0.383	0.176	0.363

Table 8. Low tide accuracy assessment results without ground control (units are in meters).

<b>Point ID</b>	<b>Error X</b>	<b>Error Y</b>	<b>Error Z</b>
Checkpoint 1	0.383	0.096	0.633
Checkpoint 2	0.230	0.259	0.608
Checkpoint 4	0.330	-0.466	-0.216
Checkpoint 5	0.481	-0.504	-0.322
<b>Mean Error</b>	0.356	-0.154	0.176
<b>Sigma</b>	0.091	0.337	0.447
<b>RMSE</b>	0.367	0.370	0.480



Figure 1. Study Area: Kimages Creek 37°19'36.8"N, 77°12'16.0"W.



Figure 2. Examples of positioned targets and photo identifiable structures used for survey coordinates of control points in Pix4D.

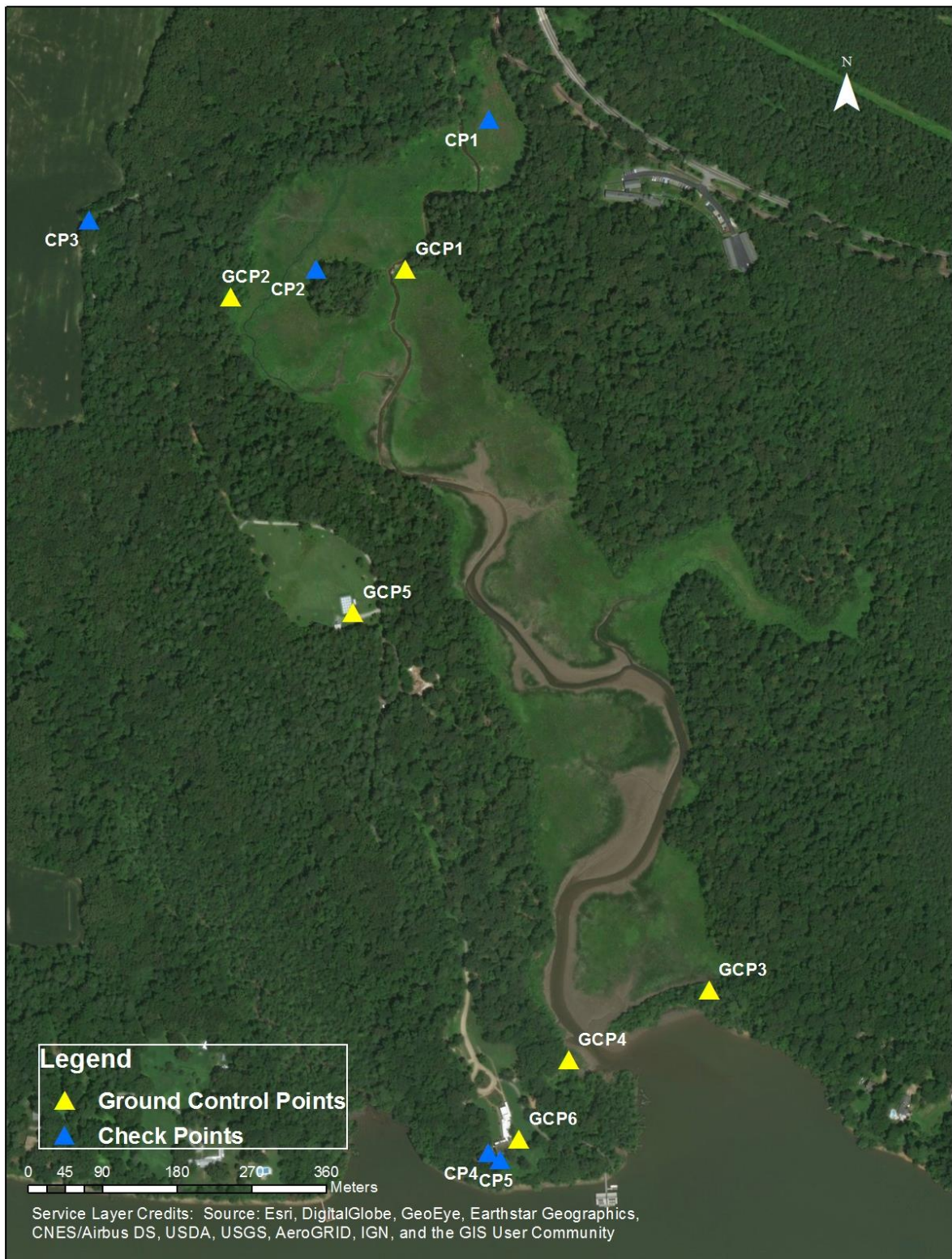


Figure 3. Ground control points (Yellow) and check points (Blue) used for high tide dataset.

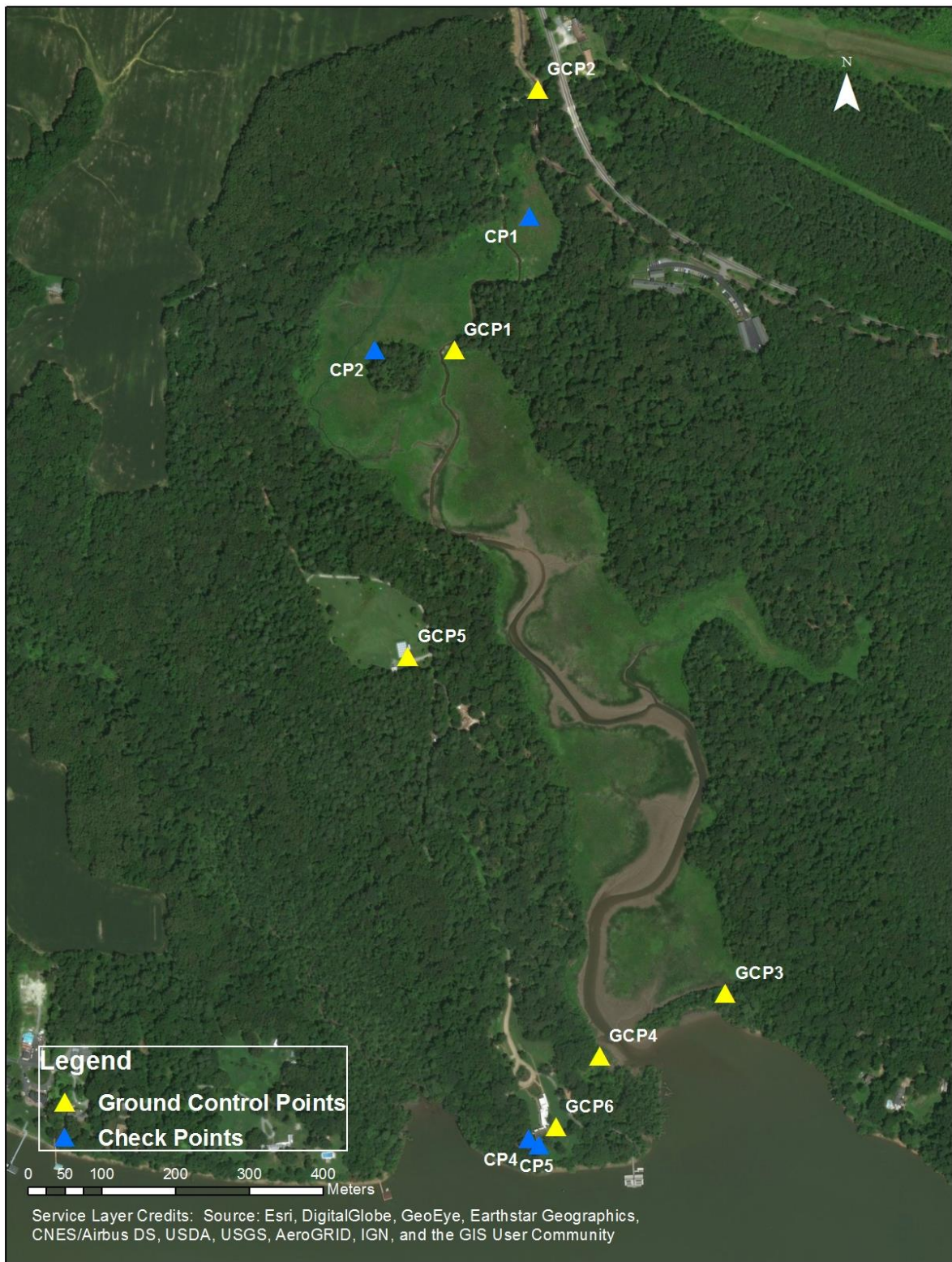


Figure 4. Ground control points (Yellow) and check points (Blue) used for low tide dataset.

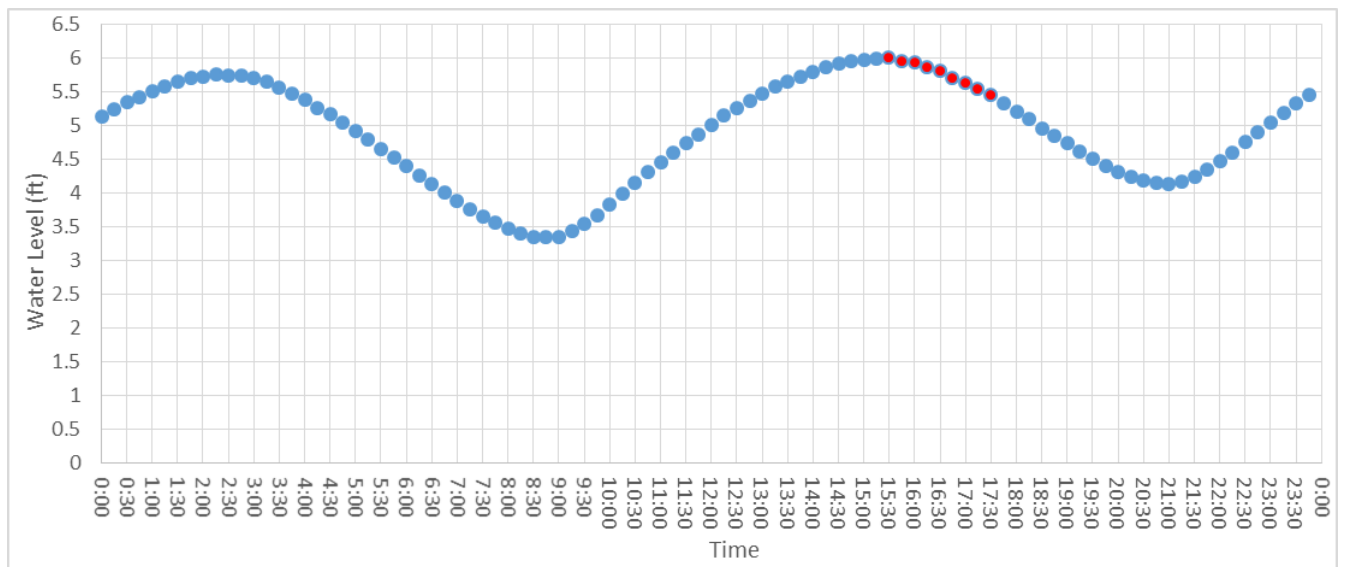


Figure 5. High tide collection on 6/7/2017. Points in red indicate flight time. Water level was collected in North American Vertical Datum 1988 feet every 15 minutes from VCU Rice Rivers Center pier gauge station. For additional information, contact the Center at: <https://ricerivers.vcu.edu/>

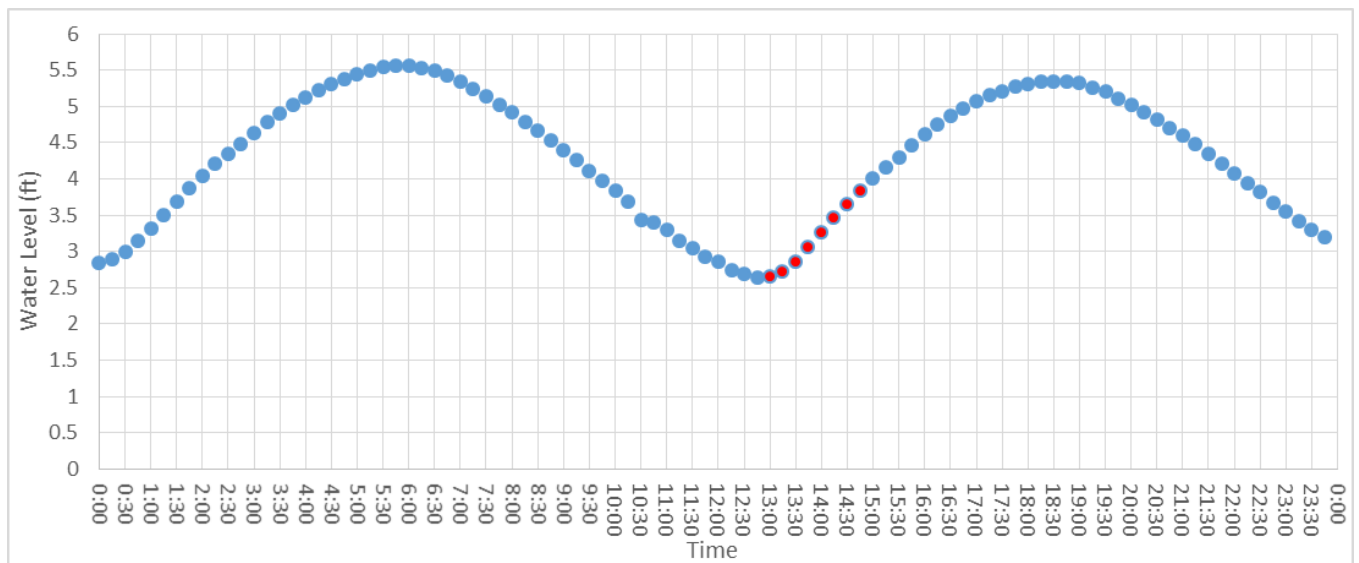


Figure 6. Low tide collection on 7/26/2017. Points in red indicate flight time. Water level was collected in North American Vertical Datum 1988 feet every 15 minutes from VCU Rice Rivers Center pier gauge station. For additional information, contact the Center at: <https://ricerivers.vcu.edu/>

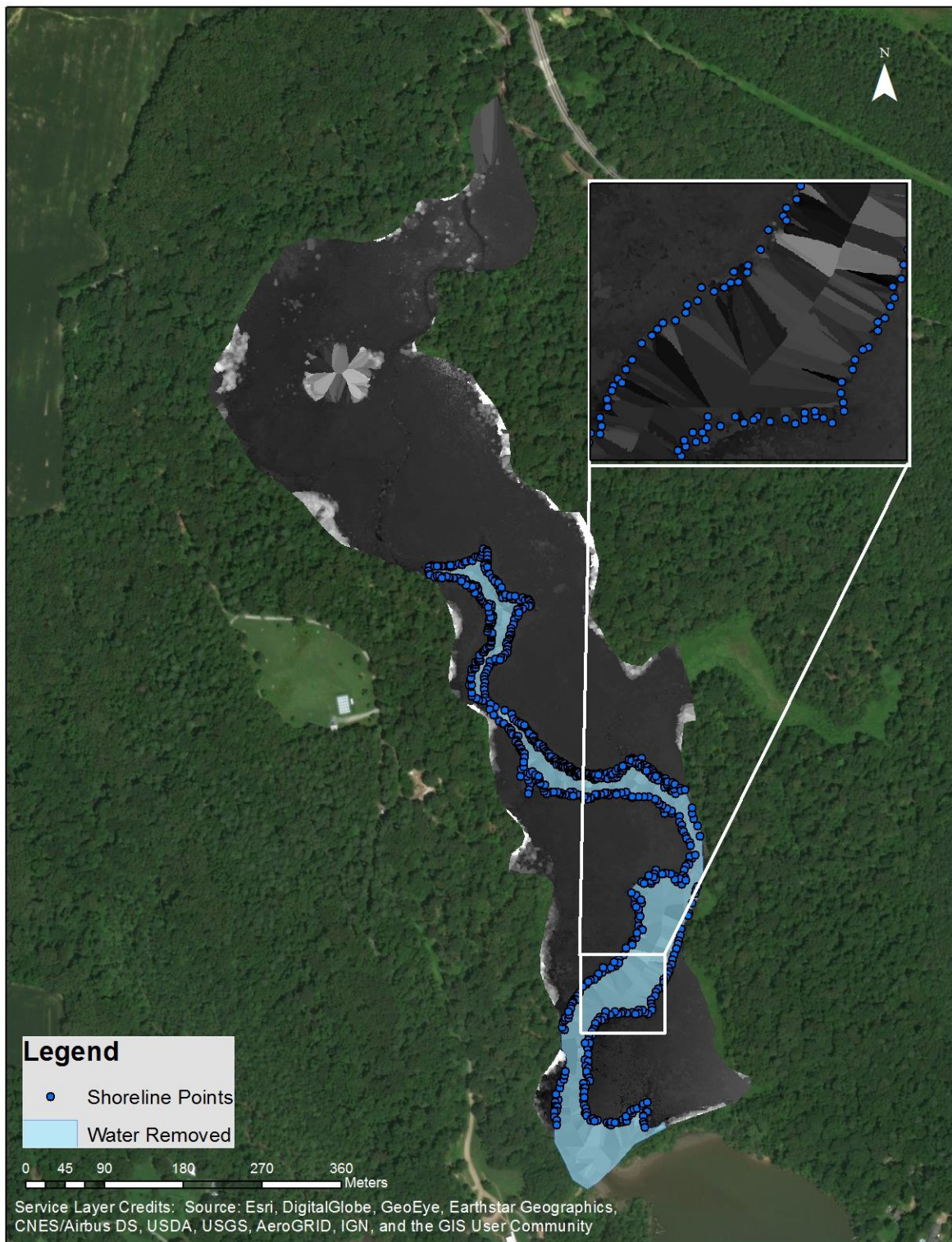


Figure 7. Shoreline points used to create continuous water surface elevation, and mask showing area of elevation model removed from high and low tide.

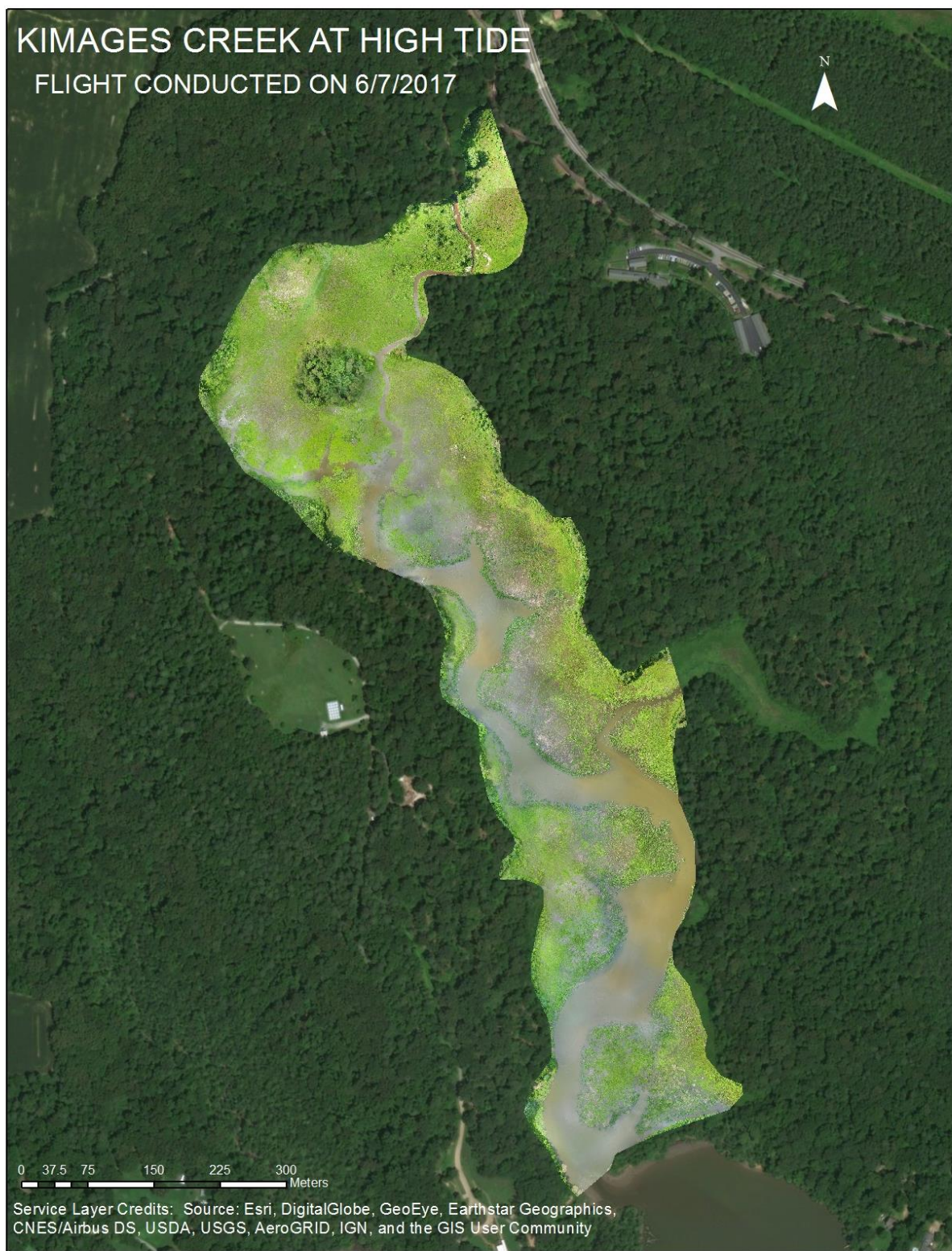


Figure 8. High tide orthophoto created with ground control points.



Figure 9. Low tide orthophoto created with ground control points.

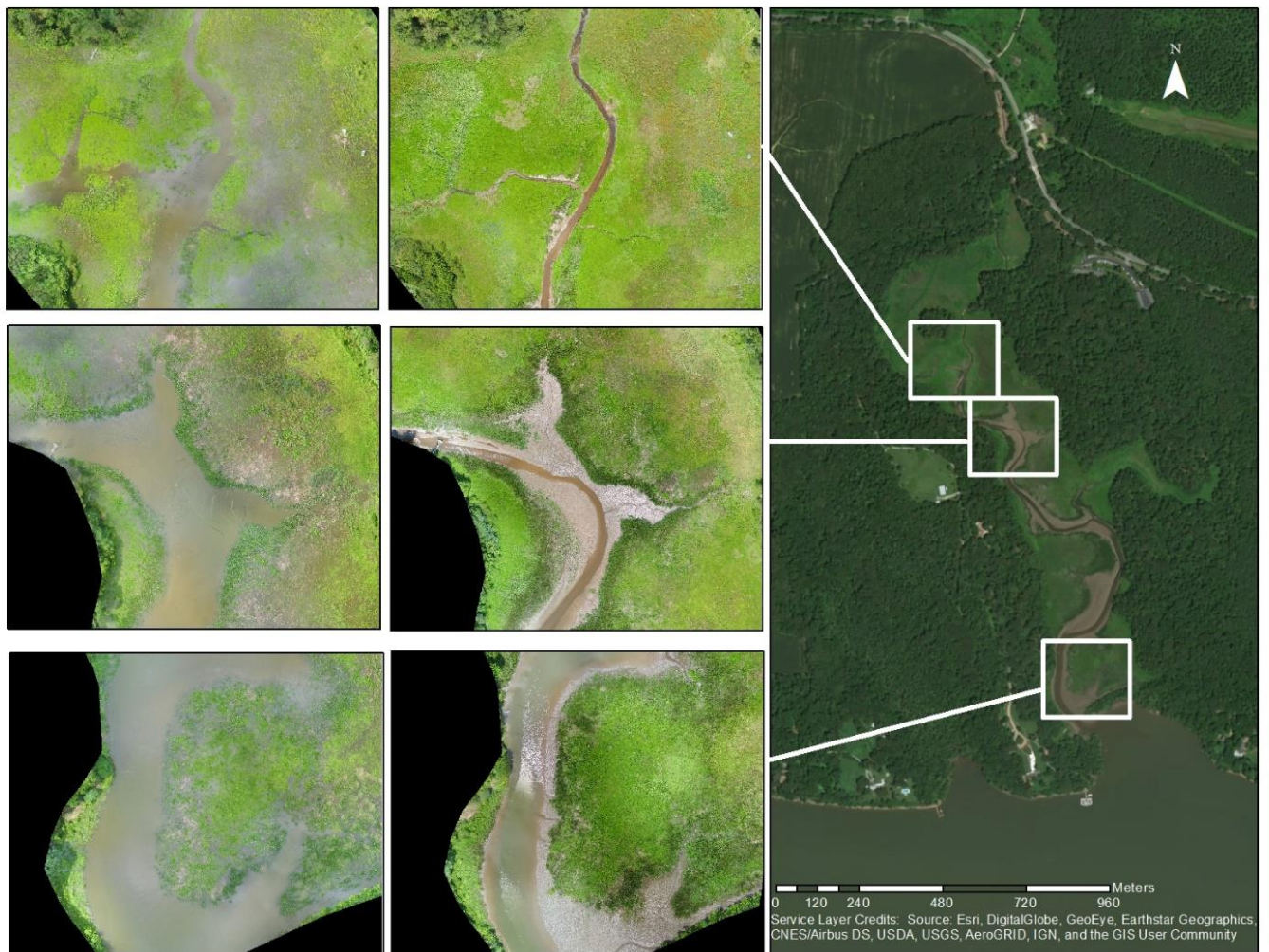
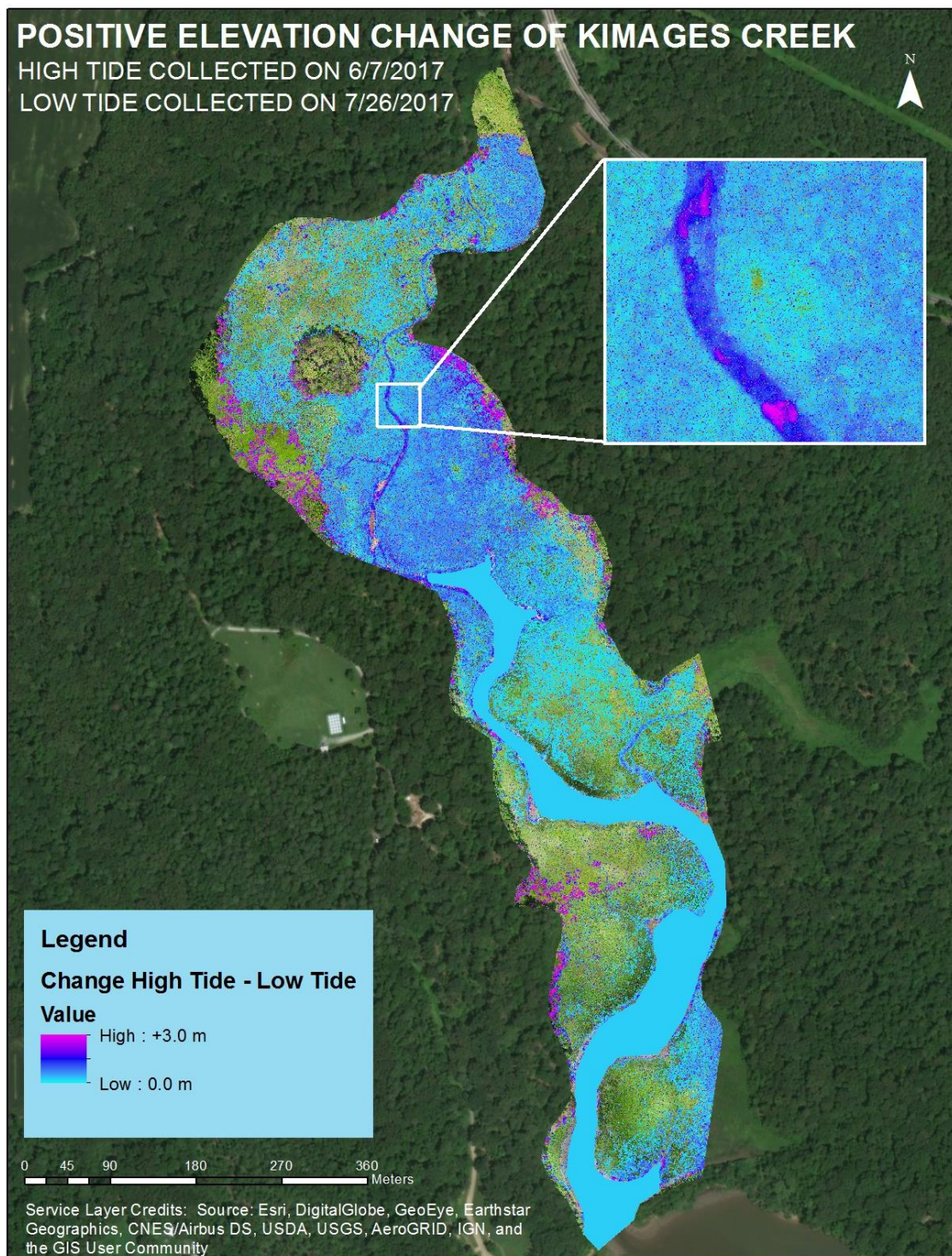


Figure 10. Inset views of high tide (left) and low tide (right).



**Figure 11.** The extent of high tide elevation above the low tide elevation. The final output is displayed above the low tide orthophoto to depict change.

## Image Processing

High tide report with incorporated GCPs.

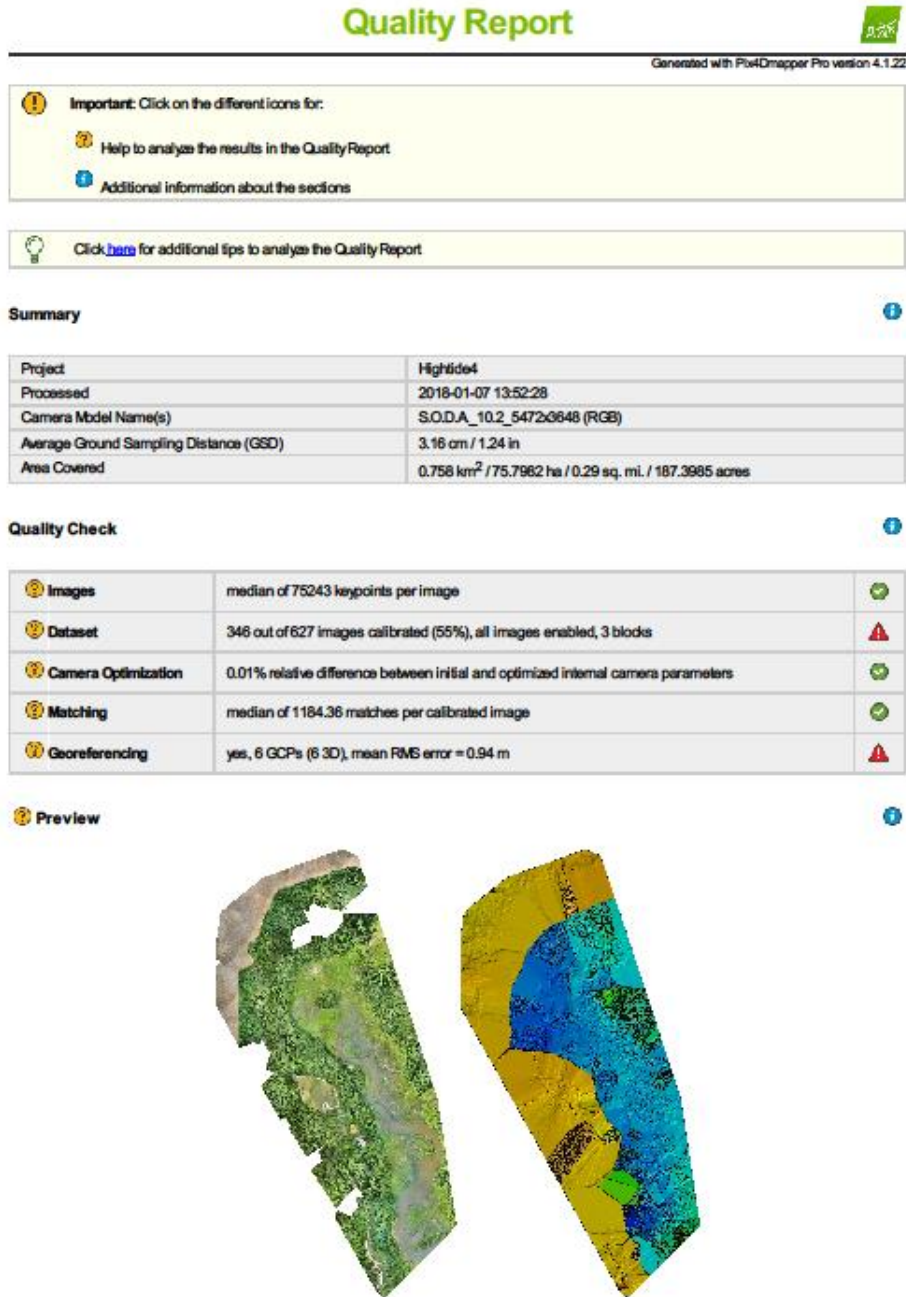


Figure 1: Orthomosaic and the corresponding sparse Digital Surface Model (DSM) before densification.

# Calibration Details

Number of Calibrated Images	346 out of 627
Number of Geolocated Images	627 out of 627

## Initial Image Positions

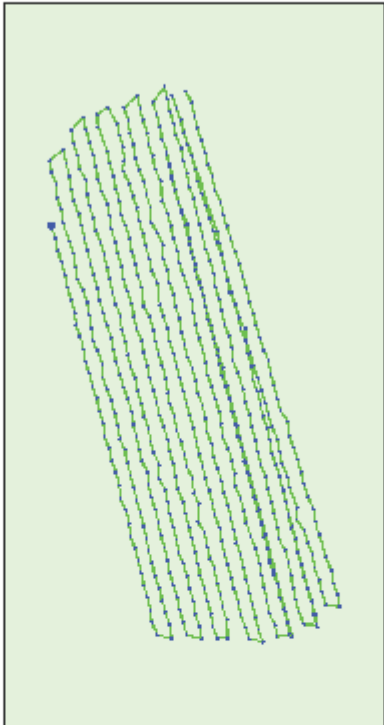


Figure 2: Top view of the initial image position. The green line follows the position of the images in time starting from the large blue dot.

## Computed Image/GCPs/Manual Tie Points Positions

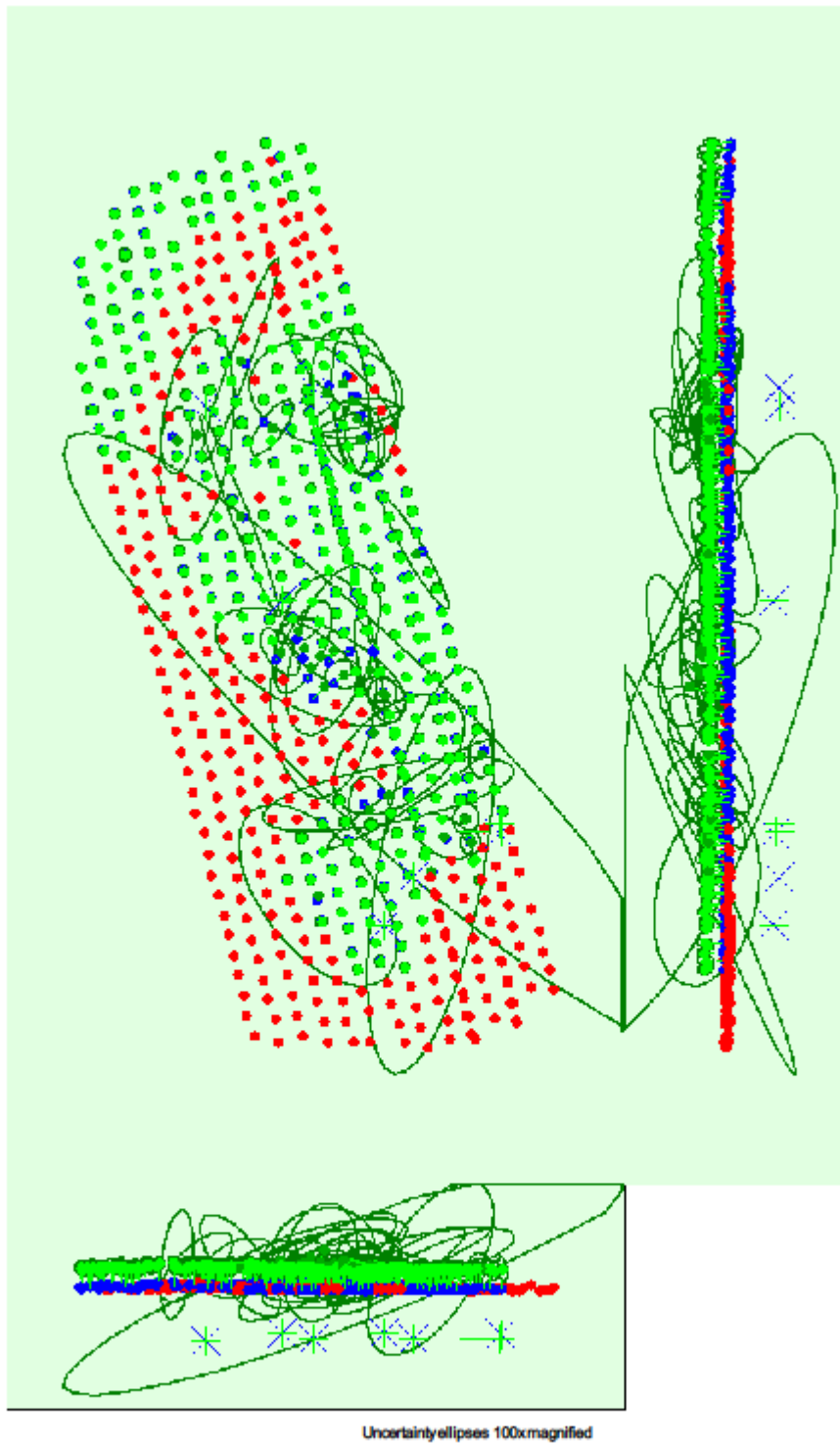


Figure 3: Offset between initial (blue dots) and computed (green dots) image positions as well as the offset between the GCPs initial positions (blue crosses) and their computed positions (green crosses) in the top-view (XY plane), front-view (XZ plane), and side-view (YZ plane). Red dots indicate disabled or uncalibrated images. Dark green ellipses indicate the absolute position uncertainty of the bundle block adjustment result.

#### Absolute camera position and orientation uncertainties



	X[m]	Y[m]	Z[m]	Omega [degree]	Phi [degree]	Kappa [degree]
Mean	0.177	0.198	0.181	0.105	0.101	0.090
Sigma	0.414	0.483	0.216	0.176	0.194	0.119

#### Overlap

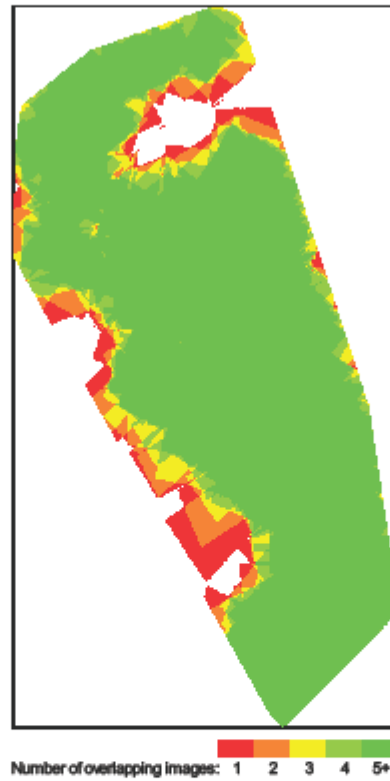


Figure 4: Number of overlapping images computed for each pixel of the orthomosaic. Red and yellow areas indicate low overlap for which poor results may be generated. Green areas indicate an overlap of over 5 images for every pixel. Good quality results will be generated as long as the number of keypoint matches is also sufficient for these areas (see Figure 5 for keypoint matches).

## Bundle Block Adjustment Details



Number of 2D Keypoint Observations for Bundle Block Adjustment	522708
Number of 3D Points for Bundle Block Adjustment	227592
Mean Reprojection Error [pixels]	0.164

#### Internal Camera Parameters

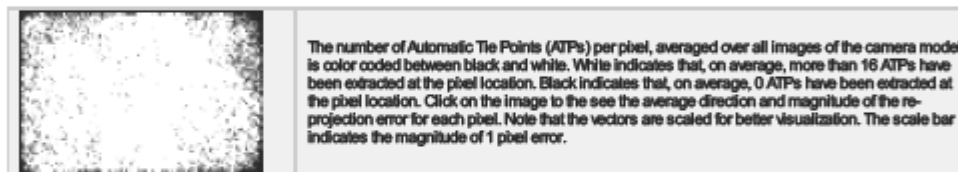
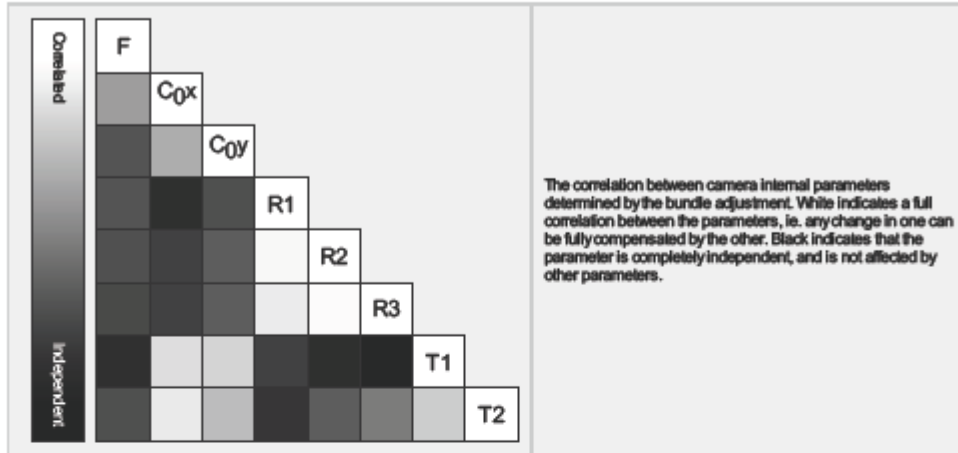
 S.O.D.A.\_10.2\_5472x3648 (RGB). Sensor Dimensions: 13.132 [mm] x 8.755 [mm]



EXIF ID: S.O.D.A.\_10.2\_5472x3648

	Focal Length	Principal Point x	Principal Point y	R1	R2	R3	T1	T2
--	--------------	-------------------	-------------------	----	----	----	----	----

Initial Values	4383.639 [pixel] 10.520 [mm]	2684.442 [pixel] 6.442 [mm]	1818.911 [pixel] 4.365 [mm]	-0.121	-0.192	0.262	-0.000	-0.002
Optimized Values	4384.463 [pixel] 10.522 [mm]	2744.726 [pixel] 6.587 [mm]	1778.575 [pixel] 4.268 [mm]	0.120	-0.421	0.380	-0.002	-0.001
Uncertainties (Sigma)	2.282 [pixel] 0.005 [mm]	1.882 [pixel] 0.005 [mm]	1.652 [pixel] 0.004 [mm]	0.003	0.012	0.016	0.000	0.000



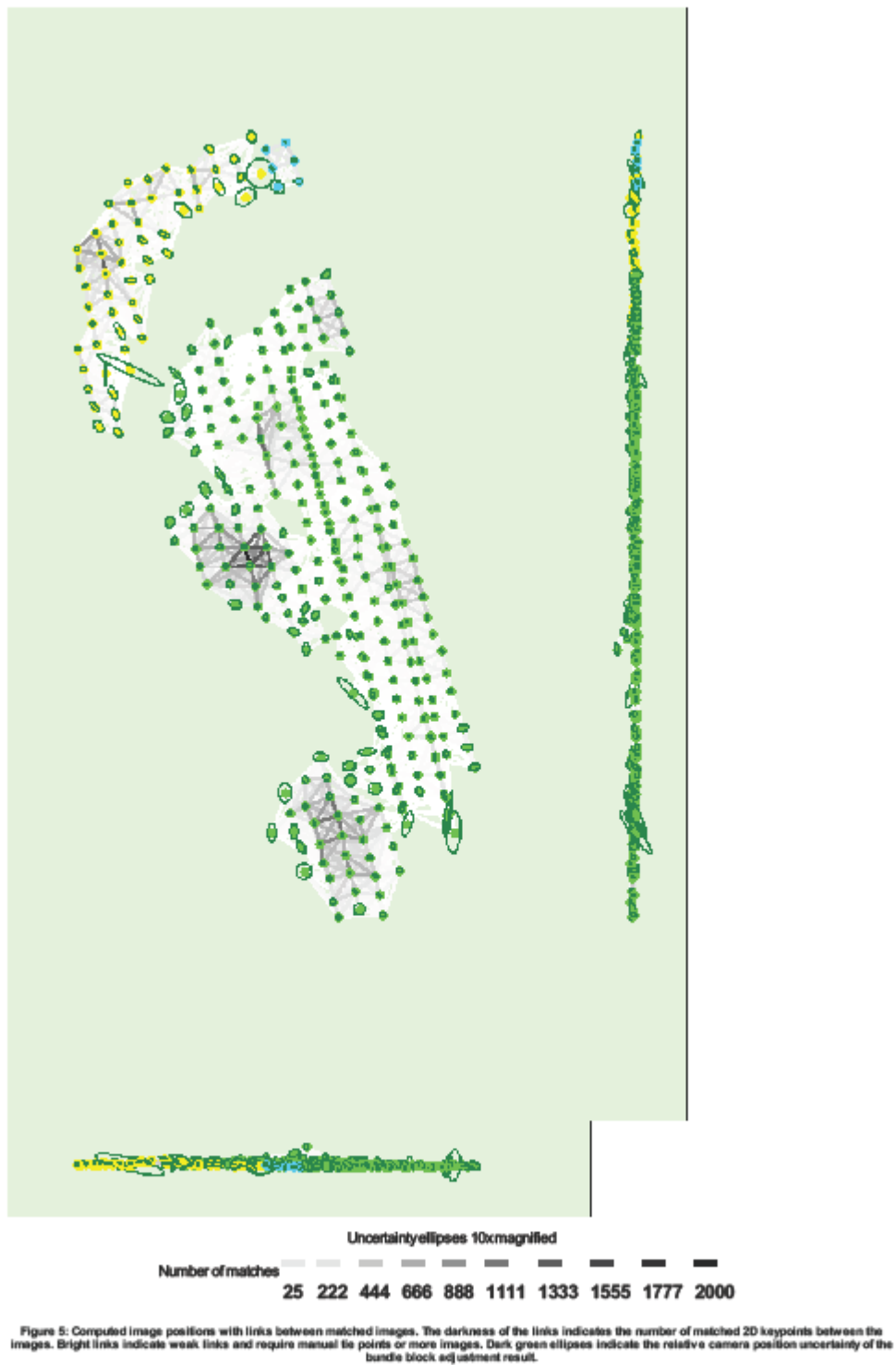
## 2D Keypoints Table

	Number of 2D Keypoints per Image	Number of Matched 2D Keypoints per Image
Median	75243	1184
Min	26933	32
Max	87827	8283
Mean	71567	1511

## 3D Points from 2D Keypoint Matches

	Number of 3D Points Observed
In 2 Images	187459
In 3 Images	25749
In 4 Images	7727
In 5 Images	3371
In 6 Images	1643
In 7 Images	858
In 8 Images	407
In 9 Images	201
In 10 Images	117
In 11 Images	44
In 12 Images	13
In 13 Images	3

## 2D Keypoint Matches



Relative camera position and orientation uncertainties



	X[m]	Y[m]	Z[m]	Omega [degree]	Phi [degree]	Kappa [degree]
Mean	0.577	0.643	0.564	0.314	0.288	0.134
Sigma	0.521	0.558	0.345	0.278	0.216	0.120

## Manual Tie Points

MTP Name	Projection Error [pixel]	Verified/Marked
mp12	1.376	5 / 5
mp13	1.513	12 / 13

Projection errors for manual tie points. The last column counts the number of images where the manual tie point has been automatically verified vs. manually marked.

## Geolocation Details

### Ground Control Points

GCP Name	Accuracy XYZ [m]	Error X [m]	Error Y [m]	Error Z [m]	Projection Error [pixel]	Verified/Marked
After_Island (3D)	0.020/0.020	0.056	-0.034	-0.038	0.772	10 / 10
Before_Island (3D)	0.020/0.020	0.042	0.152	0.088	7.046	10 / 10
Breach2 (3D)	0.020/0.020	-1.379	-1.346	4.762	23.058	4 / 4
Before_Breach (3D)	0.020/0.020	-0.081	-0.113	-0.187	3.182	6 / 6
Shed1 (3D)	0.020/0.020	-0.027	0.035	-0.011	1.390	11 / 11
Front_MainBuilding (3D)	0.020/0.020	0.019	0.027	-0.044	0.704	12 / 12
Mean [m]		-0.228218	-0.213323	0.761719		
Sigma [m]		0.516527	0.512862	1.790858		
RMS Error [m]		0.564698	0.555458	1.946121		

0 out of 5 check points have been labeled as inaccurate.

Check Point Name	Accuracy XYZ [m]	Error X [m]	Error Y [m]	Error Z [m]	Projection Error [pixel]	Verified/Marked
Top_Arm		-0.5410	-0.3113	-0.3288	0.2776	8 / 8
Island		0.3061	-0.0491	0.2972	1.0458	9 / 10
Powerline		-0.4099	-0.2082	0.1818	0.8932	5 / 5
Side_MainBuilding		0.0722	-0.4099	0.0316	0.5706	4 / 4
Behind_MainBuilding		0.1721	-0.0815	-0.1978	0.2460	6 / 6
Mean [m]		-0.080121	-0.211991	-0.003213		
Sigma [m]		0.333809	0.136092	0.232182		
RMS Error [m]		0.343290	0.251915	0.232205		

Localisation accuracy per GCP and mean errors in the three coordinate directions. The last column counts the number of calibrated images where the GCP has been automatically verified vs. manually marked.

### Absolute Geolocation Variance

Min Error [m]	Max Error [m]	Geolocation Error X [%]	Geolocation Error Y [%]	Geolocation Error Z [%]
-	-0.08	0.32	0.00	15.21
-0.08	-0.06	0.32	0.00	2.59
-0.06	-0.05	0.65	0.00	3.88
-0.05	-0.03	2.27	2.59	4.21
-0.03	-0.02	6.80	6.80	6.47
-0.02	0.00	35.28	42.07	18.12
0.00	0.02	46.60	39.48	11.00
0.02	0.03	6.47	7.12	5.50
0.03	0.05	0.97	1.94	2.59

0.05	0.06	0.00	0.00	4.85
0.06	0.08	0.00	0.00	5.50
0.08	-	0.32	0.00	20.06
Mean [m]		-0.610630	0.751327	-36.703457
Sigma [m]		0.015586	0.013323	0.165599
RMS Error [m]		0.610829	0.751445	36.703830

Min Error and Max Error represent geolocation error intervals between -1.5 and 1.5 times the maximum accuracy of all the images. Columns X, Y, Z show the percentage of images with geolocation errors within the predefined error intervals. The geolocation error is the difference between the initial and computed image positions. Note that the image geolocation errors do not correspond to the accuracy of the observed 3D points.

Geolocation Bias	X	Y	Z
Translation [m]	-0.610492	0.751608	-36.705800

Bias between image initial and computed geolocation given in output coordinate system.

## Relative Geolocation Variance

Relative Geolocation Error	Images X [%]	Images Y [%]	Images Z [%]
[-1.00, 1.00]	77.02	77.87	36.57
[-2.00, 2.00]	92.56	93.20	50.49
[-3.00, 3.00]	97.41	98.71	64.40
Mean of Geolocation Accuracy [m]	0.014070	0.014070	0.029165
Sigma of Geolocation Accuracy [m]	0.001961	0.001961	0.008319

Images X, Y, Z represent the percentage of images with a relative geolocation error in X, Y, Z.

Geolocation Orientation Variance	RMS [degree]
Omega	5.179
Phi	7.215
Kappa	9.754

Geolocation RMS error of the orientation angles given by the difference between the initial and computed image orientation angles.

## Initial Processing Details

### System Information

Hardware	CPU: Intel(R) Xeon(R) CPU E5-1620 v3 @ 3.50GHz RAM: 32GB GPU: NVIDIA Quadro K5200 (Driver: 21.21.13.6939), RDPDD Chained DD (Driver: unknown), RDP Encoder Mirror Driver (Driver: unknown), RDP Reflector Display Driver (Driver: unknown)
Operating System	Windows 7 Enterprise, 64-bit

### Coordinate Systems

Image Coordinate System	WGS84
Ground Control Point (GCP) Coordinate System	NAD83 / UTM zone 18N
Output Coordinate System	NAD83 / UTM zone 18N

### Processing Options

Detected Template	H 3D Maps
Keypoints Image Scale	Full, Image Scale: 1
Advanced: Matching Image Pairs	Aerial Grid or Corridor
Advanced: Matching Strategy	Use Geometrically Verified Matching: no

Advanced: Keypoint Extraction	Targeted Number of Keypoints: Automatic
Advanced: Calibration	Calibration Method: Standard Internal Parameters Optimization: All External Parameters Optimization: All Rematch: Auto, no

## Point Cloud Densification details

### Processing Options

Image Scale	multiscale, 1/2 (Half image size, Default)
Point Density	Optimal
Minimum Number of Matches	3
3D Textured Mesh Generation	yes
3D Textured Mesh Settings:	Resolution: Medium Resolution (default) Color Balancing: no
LOD	Generated: no
Advanced: 3D Textured Mesh Settings	Sample Density Divider: 1
Advanced: Image Groups	group1
Advanced: Use Processing Area	yes
Advanced: Use Annotations	yes
Time for Point Cloud Densification	39m:36s
Time for Point Cloud Classification	NA
Time for 3D Textured Mesh Generation	10m:52s

### Results

Number of Generated Tiles	1
Number of 3D Densified Points	27226738
Average Density (per m <sup>3</sup> )	83.8

## DSM, Orthomosaic and Index Details

### Processing Options

DSM and Orthomosaic Resolution	1 x GSD (3.16 [cm/pixel])
DSM Filters	Noise Filtering: yes Surface Smoothing: yes, Type: Sharp
Raster DSM	Generated: yes Method: Inverse Distance Weighting Merge Tiles: yes
Orthomosaic	Generated: yes Merge Tiles: yes GeoTIFF Without Transparency: no Google Maps Tiles and KML: no
Time for DSM Generation	02h:26m:05s
Time for Orthomosaic Generation	53m:04s
Time for DTM Generation	00s
Time for Contour Lines Generation	00s
Time for Reflectance Map Generation	00s
Time for Index Map Generation	00s

High tide report without incorporated GCPs.



Figure 1: Orthomosaic and the corresponding sparse Digital Surface Model (DSM) before densification.

## Calibration Details



Number of Calibrated Images	345 out of 627
Number of Geolocated Images	627 out of 627

### Initial Image Positions

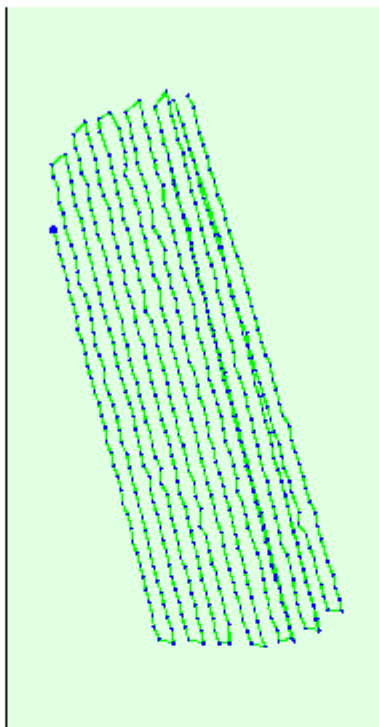


Figure 2: Top view of the initial image position. The green line follows the position of the images in time starting from the large blue dot.

### Computed Image/GCPs/Manual Tie Points Positions



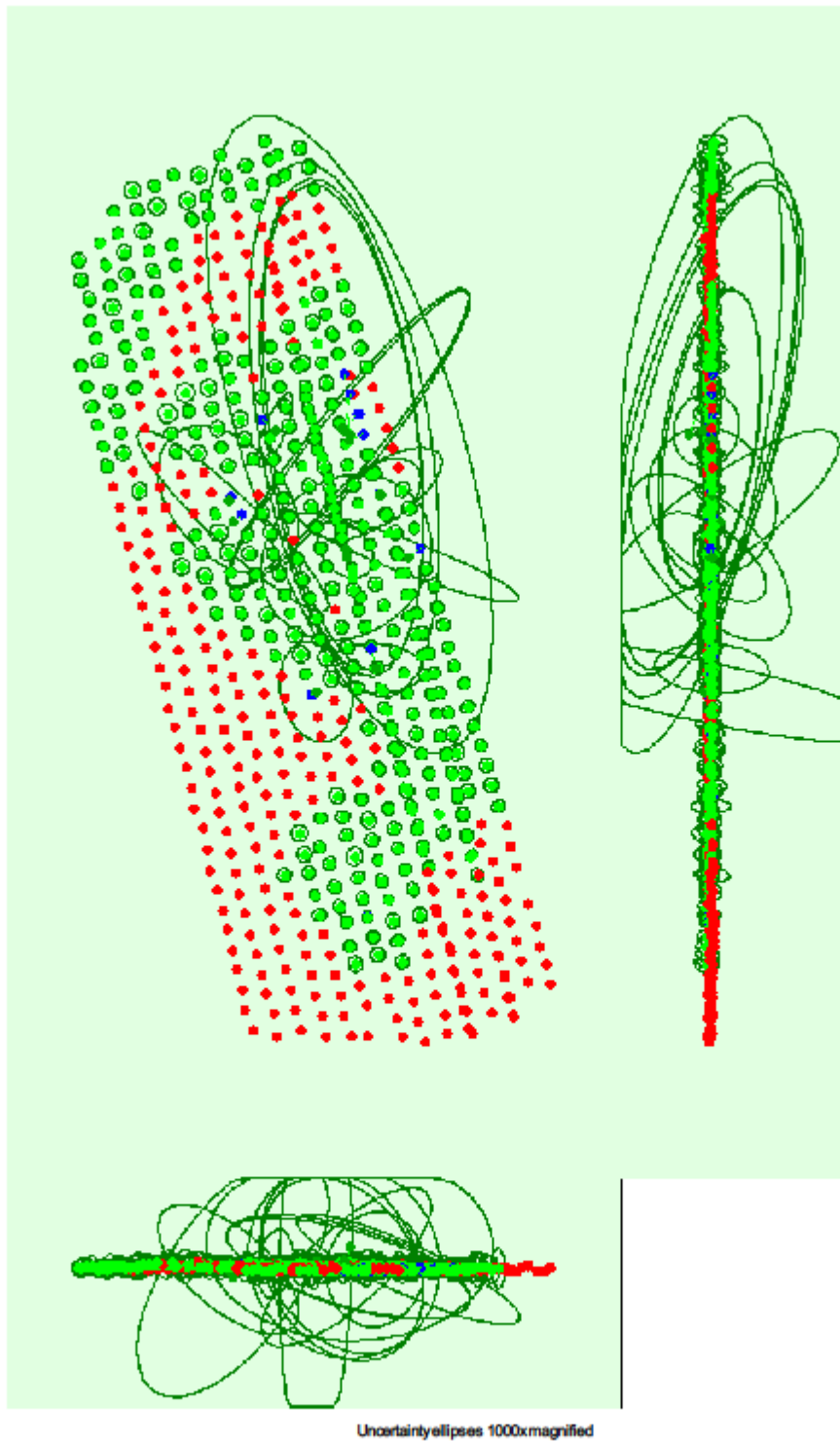


Figure 3: Offset between initial (blue dots) and computed (green dots) image positions as well as the offset between the GCPs initial positions (blue crosses) and their computed positions (green crosses) in the top-view (XY plane), front-view (XZ plane), and side-view (YZ plane). Red dots indicate disabled or uncalibrated images. Dark green ellipses indicate the absolute position uncertainty of the bundle block adjustment result.

#### Absolute camera position and orientation uncertainties



	X[m]	Y[m]	Z[m]	Omega [degree]	Phi [degree]	Kappa [degree]
Mean	0.019	0.023	0.023	0.018	0.018	0.018
Sigma	0.033	0.062	0.033	0.021	0.025	0.020

#### Overlap

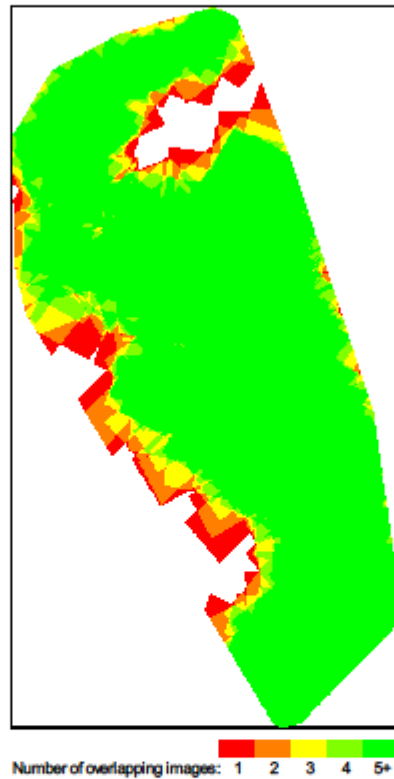



Figure 4: Number of overlapping images computed for each pixel of the orthomosaic. Red and yellow areas indicate low overlap for which poor results may be generated. Green areas indicate an overlap of over 5 images for every pixel. Good quality results will be generated as long as the number of keypoint matches is also sufficient for these areas (see Figure 5 for keypoint matches).

## Bundle Block Adjustment Details



Number of 2D Keypoint Observations for Bundle Block Adjustment	516102
Number of 3D Points for Bundle Block Adjustment	224826
Mean Reprojection Error [pixels]	0.142

#### Internal Camera Parameters

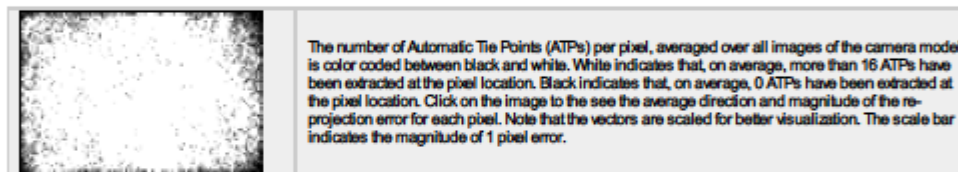
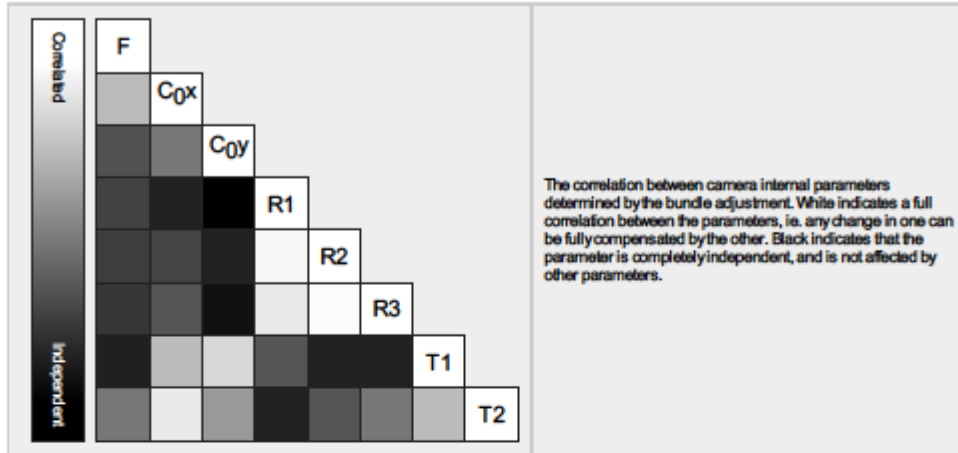
 S.O.D.A.\_10.2\_5472x3648 (RGB). Sensor Dimensions: 13.132 [mm] x 8.755 [mm]



EXIF ID: S.O.D.A.\_10.2\_5472x3648

	Focal Length	Principal Point x	Principal Point y	R1	R2	R3	T1	T2
--	--------------	-------------------	-------------------	----	----	----	----	----

Initial Values	4383.639 [pixel] 10.520 [mm]	2684.442 [pixel] 6.442 [mm]	1818.911 [pixel] 4.365 [mm]	-0.121	-0.192	0.262	-0.000	-0.002
Optimized Values	4383.016 [pixel] 10.518 [mm]	2745.942 [pixel] 6.590 [mm]	1775.758 [pixel] 4.261 [mm]	0.120	-0.421	0.382	-0.002	-0.001
Uncertainties (Sigma)	0.439 [pixel] 0.001 [mm]	0.344 [pixel] 0.001 [mm]	0.317 [pixel] 0.001 [mm]	0.000	0.002	0.003	0.000	0.000



## 2D Keypoints Table

	Number of 2D Keypoints per Image	Number of Matched 2D Keypoints per Image
Median	75102	1193
Mn	26933	33
Max	87827	9294
Mean	71463	1496

## 3D Points from 2D Keypoint Matches

	Number of 3D Points Observed
In 2 Images	185113
In 3 Images	25449
In 4 Images	7757
In 5 Images	3352
In 6 Images	1635
In 7 Images	818
In 8 Images	351
In 9 Images	194
In 10 Images	101
In 11 Images	38
In 12 Images	14
In 13 Images	3
In 16 Images	1

## 2D Keypoint Matches

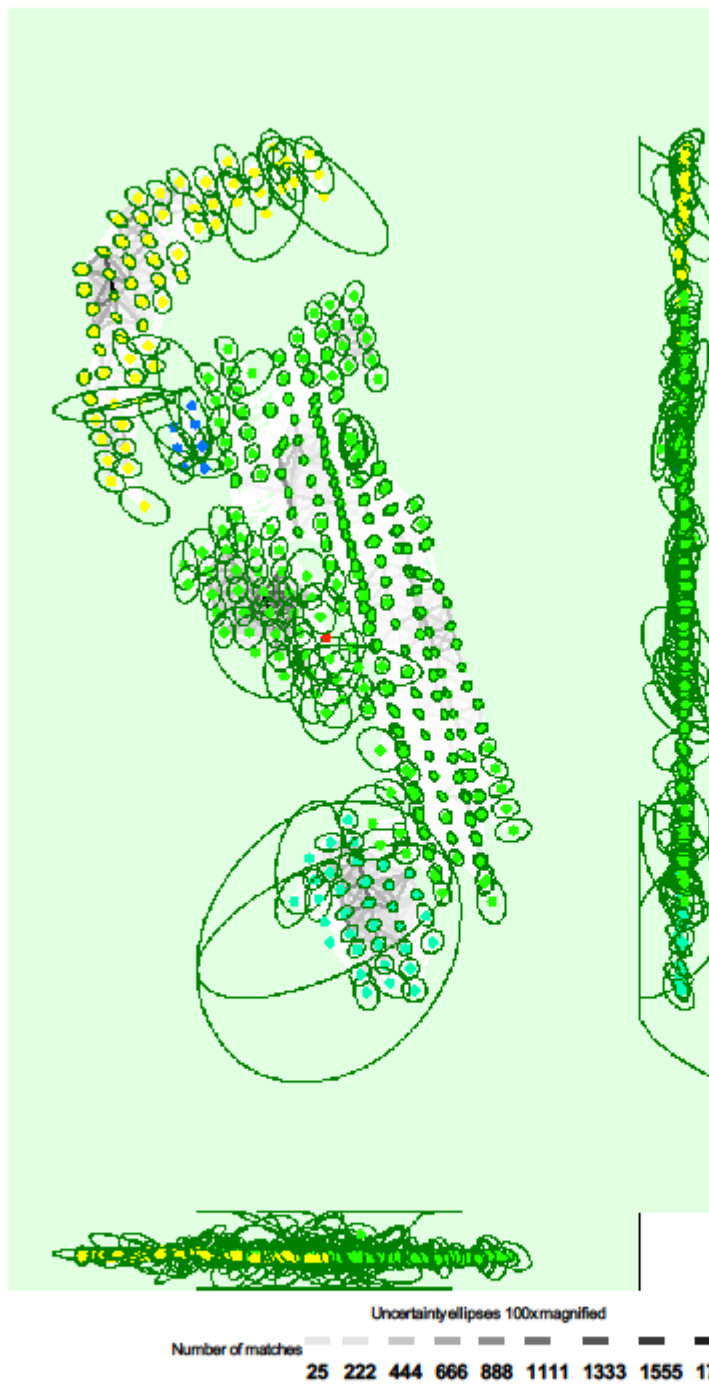



Figure 5: Computed image positions with links between matched images. The darkness of the links indicates the number of matched 2D keypoints between the images. Bright links indicate weak links and require manual tie points or more images. Dark green ellipses indicate the relative camera position uncertainty of the bundle block adjustment result.

 Relative camera position and orientation uncertainties



	X[m]	Y[m]	Z[m]	Omega [degree]	Phi [degree]	Kappa [degree]
Mean	0.208	0.226	0.201	0.113	0.112	0.051
Sigma	0.235	0.222	0.186	0.101	0.113	0.065

## Geolocation Details

### Ground Control Points

0 out of 5 check points have been labeled as inaccurate.

Check Point Name	Accuracy XYZ [m]	Error X [m]	Error Y [m]	Error Z [m]	Projection Error [pixel]	Verified/Marked
Top_Arm		0.354	-0.101	1.606	0.319	5 / 5
Island		0.672	0.135	1.594	0.799	4 / 4
Powerline		-0.010	-0.085	1.944	0.353	3 / 3
Side_MainBuilding		-0.119	-0.219	1.958	0.444	3 / 3
Behind_MainBuilding		0.219	-0.035	1.685	0.278	4 / 4
Mean [m]		0.223298	-0.060746	1.757297		
Sigma [m]		0.279377	0.115224	0.161468		
RMS Error [m]		0.357650	0.130256	1.764699		

Localisation accuracy per GCP and mean errors in the three coordinate directions. The last column counts the number of calibrated images where the GCP has been automatically verified vs. manually marked.

### Absolute Geolocation Variance

Min Error [m]	Max Error [m]	Geolocation Error X [%]	Geolocation Error Y [%]	Geolocation Error Z [%]
-	-0.08	0.00	0.00	14.89
-0.08	-0.06	0.91	0.00	2.43
-0.06	-0.05	0.61	0.91	2.43
-0.05	-0.03	1.22	0.91	5.17
-0.03	-0.02	5.47	3.65	6.08
-0.02	0.00	42.86	46.20	14.59
0.00	0.02	42.25	41.34	16.11
0.02	0.03	4.86	6.08	8.51
0.03	0.05	1.22	0.91	4.86
0.05	0.06	0.30	0.00	1.22
0.06	0.08	0.00	0.00	3.04
0.08	-	0.30	0.00	20.67
Mean [m]		-0.000379	-0.000179	0.007379
Sigma [m]		0.015168	0.011655	0.162603
RMS Error [m]		0.015172	0.011657	0.162771

Min Error and Max Error represent geolocation error intervals between -1.5 and 1.5 times the maximum accuracy of all the images. Columns X, Y, Z show the percentage of images with geolocation errors within the predefined error intervals. The geolocation error is the difference between the initial and computed image positions. Note that the image geolocation errors do not correspond to the accuracy of the observed 3D points.

### Relative Geolocation Variance

Relative Geolocation Error	Images X [%]	Images Y [%]	Images Z [%]
[-1.00, 1.00]	79.94	86.02	41.95
[-2.00, 2.00]	93.92	95.14	54.71
[-3.00, 3.00]	96.66	98.48	65.05
Mean of Geolocation Accuracy [m]	0.014103	0.014103	0.028888

Sigma of Geolocation Accuracy [m]	0.001996	0.001996	0.006168
-----------------------------------	----------	----------	----------

Images X, Y, Z represent the percentage of images with a relative geolocation error in X, Y, Z.

Geolocation Orientational Variance	RMS [degree]
Omega	5.068
Phi	7.302
Kappa	10.069

Geolocation RMS error of the orientation angles given by the difference between the Initial and computed image orientation angles.

## Initial Processing Details


### System Information

Hardware	CPU: Intel(R) Xeon(R) CPU E5-1620 v3 @ 3.50GHz RAM: 32GB GPU: NVIDIA Quadro K5200 (Driver: 21.21.13.6939), RDPDD Chained DD (Driver: unknown), RDP Encoder Mirror Driver (Driver: unknown), RDP Reflector Display Driver (Driver: unknown)
Operating System	Windows 7 Enterprise, 64-bit

### Coordinate Systems

Image Coordinate System	WGS84
Output Coordinate System	WGS 84 / UTM zone 18N

### Processing Options

Detected Template	 3D Maps
Keypoints Image Scale	Full, Image Scale: 1
Advanced: Matching Image Pairs	Aerial Grid or Corridor
Advanced: Matching Strategy	Use Geometrically Verified Matching: no
Advanced: Keypoint Extraction	Targeted Number of Keypoints: Automatic
Advanced: Calibration	Calibration Method: Standard Internal Parameters Optimization: All External Parameters Optimization: All Rematch: Auto, no

Low tide report with incorporated GCPs.

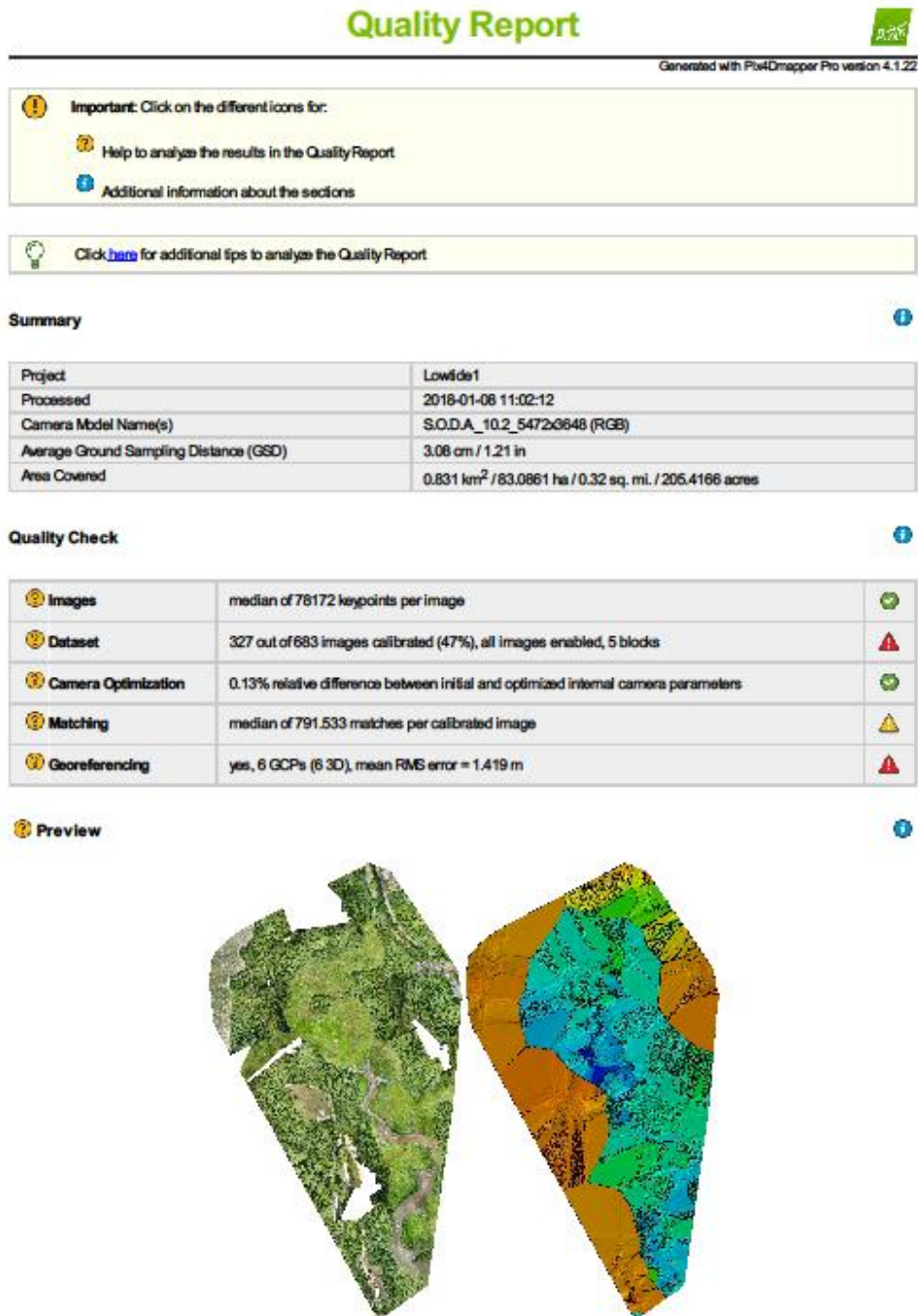


Figure 1: Orthomosaic and the corresponding sparse Digital Surface Model (DSM) before densification.

## Calibration Details



Number of Calibrated Images	327 out of 683
Number of Geolocated Images	683 out of 683

### Initial Image Positions

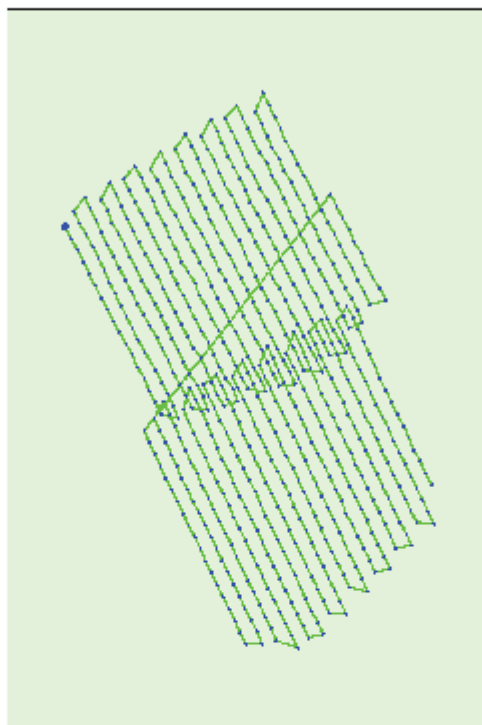


Figure 2: Top view of the initial image position. The green line follows the position of the images in time starting from the large blue dot.

### Computed Image/GCPs/Manual Tie Points Positions



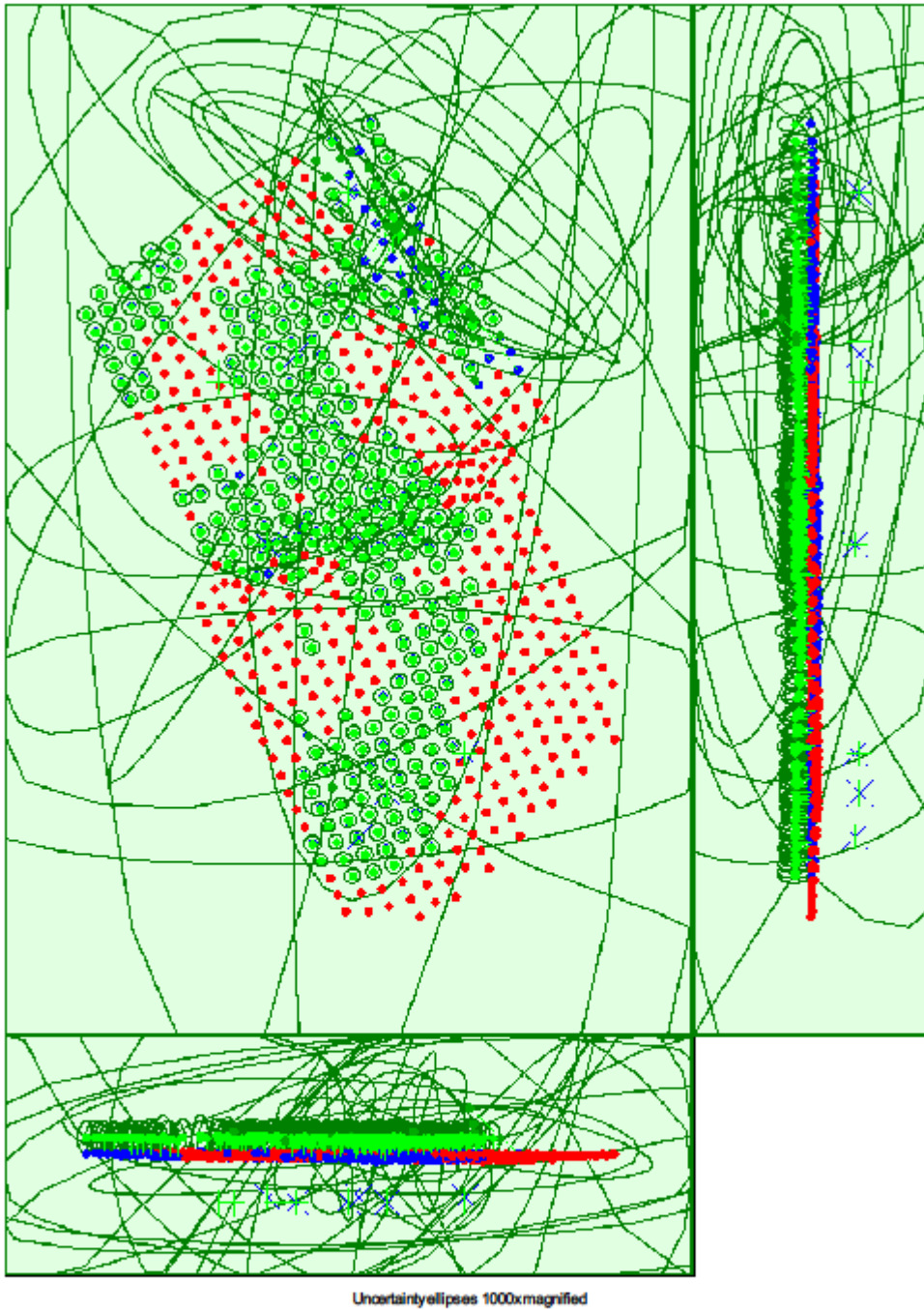


Figure 3: Offset between initial (blue dots) and computed (green dots) image positions as well as the offset between the GCPs initial positions (blue crosses) and their computed positions (green crosses) in the top-view (XY plane), front-view (XZ plane), and side-view (YZ plane). Red dots indicate disabled or uncalibrated images. Dark green ellipses indicate the absolute position uncertainty of the bundle block adjustment result.

#### Absolute camera position and orientation uncertainties



X[m]	Y[m]	Z[m]	Omega [degree]	Phi [degree]	Kappa [degree]
------	------	------	----------------	--------------	----------------

Mean	0.084	0.160	0.091	583.806	2557.851	3535.897
Sigma	0.331	0.963	0.346	8653.077	36411.485	45724.265

## Overlap

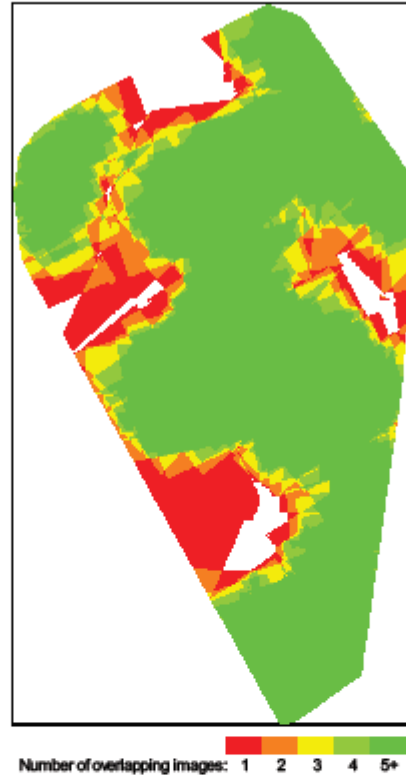


Figure 4: Number of overlapping images computed for each pixel of the orthomosaic. Red and yellow areas indicate low overlap for which poor results may be generated. Green areas indicate an overlap of over 5 images for every pixel. Good quality results will be generated as long as the number of keypoint matches is also sufficient for these areas (see Figure 5 for keypoint matches).

## Bundle Block Adjustment Details

Number of 2D Keypoint Observations for Bundle Block Adjustment	426425
Number of 3D Points for Bundle Block Adjustment	169672
Mean Reprojection Error [pixels]	0.156

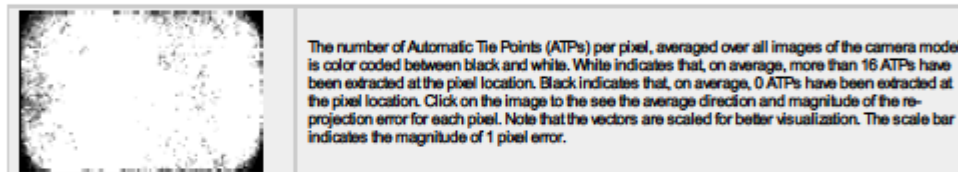
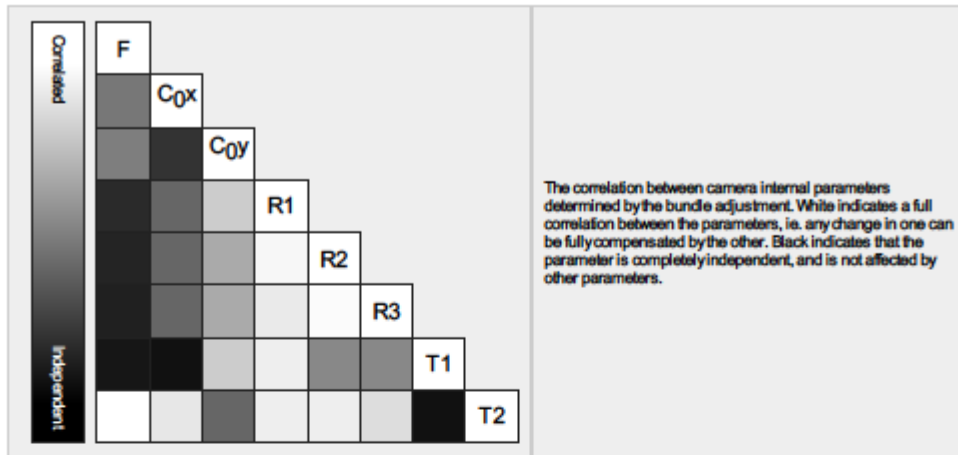
## Internal Camera Parameters

S.O.D.A.\_10.2\_5472x3648 (RGB). Sensor Dimensions: 13.132 [mm] x 8.755 [mm]

EXIF ID: S.O.D.A.\_10.2\_5472x3648

	Focal Length	Principal Point x	Principal Point y	R1	R2	R3	T1	T2
Initial Values	4383.639 [pixel] 10.520 [mm]	2684.442 [pixel] 6.442 [mm]	1818.911 [pixel] 4.365 [mm]	-0.121	-0.192	0.262	-0.000	-0.002
Optimized Values	4377.575 [pixel] 10.505 [mm]	2744.127 [pixel] 6.585 [mm]	1778.994 [pixel] 4.269 [mm]	0.114	-0.394	0.343	-0.002	-0.001

Uncertainties (Sigma)	0.825 [pixel] 0.002 [mm]	0.480 [pixel] 0.001 [mm]	0.499 [pixel] 0.001 [mm]	0.001	0.003	0.005	0.000	0.000
-----------------------	-----------------------------	-----------------------------	-----------------------------	-------	-------	-------	-------	-------



## 2D Keypoints Table

	Number of 2D Keypoints per Image	Number of Matched 2D Keypoints per Image
Median	78172	792
Min	38524	22
Max	91262	10393
Mean	76291	1304

## 3D Points from 2D Keypoint Matches

	Number of 3D Points Observed
In 2 Images	126236
In 3 Images	23859
In 4 Images	9050
In 5 Images	4805
In 6 Images	2511
In 7 Images	1438
In 8 Images	862
In 9 Images	531
In 10 Images	283
In 11 Images	149
In 12 Images	82
In 13 Images	39
In 14 Images	22
In 15 Images	4
In 16 Images	1

## 2D Keypoint Matches

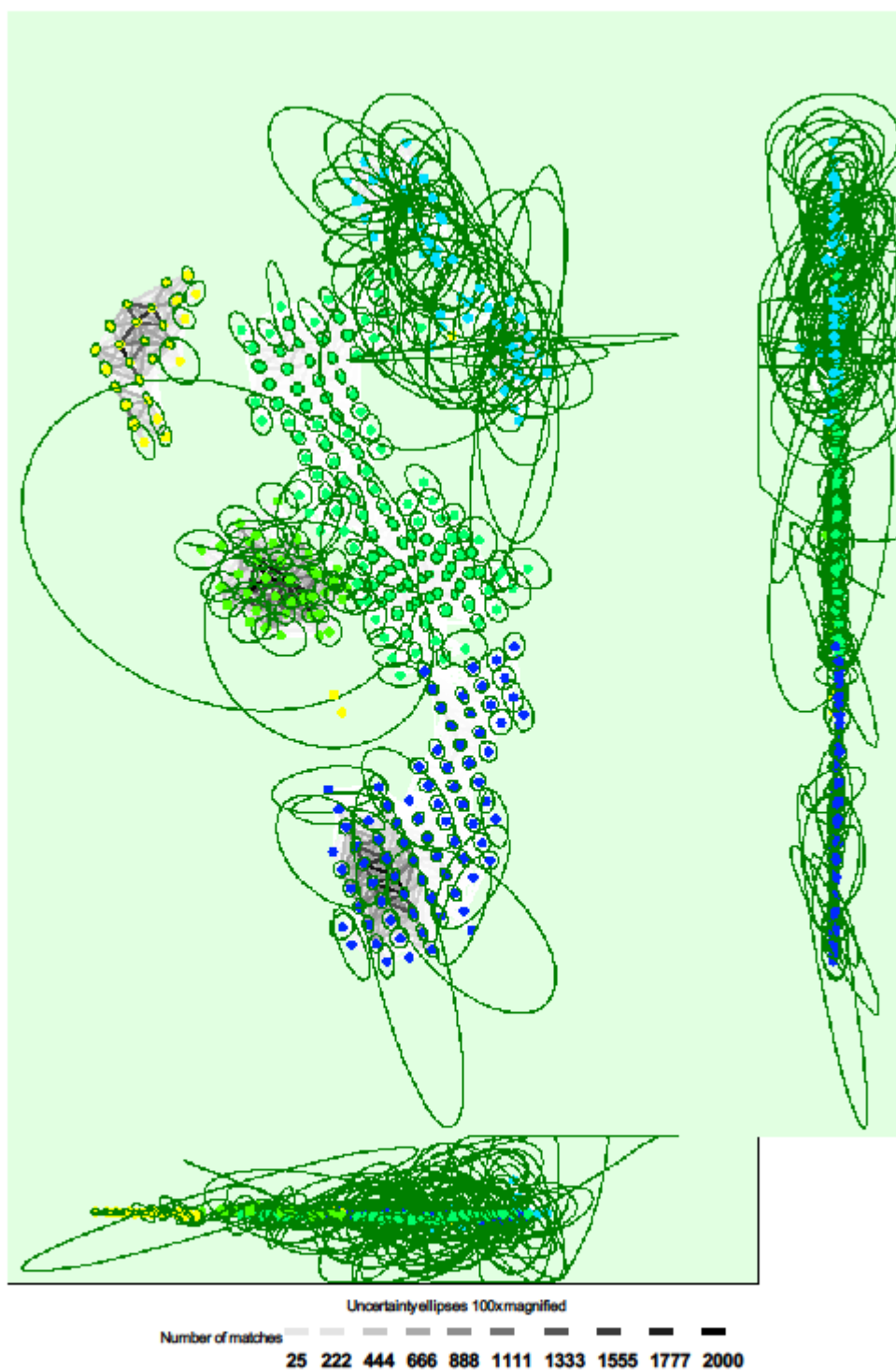


Figure 5: Computed image positions with links between matched images. The darkness of the links indicates the number of matched 2D keypoints between the images. Bright links indicate weak links and require manual tie points or more images. Dark green ellipses indicate the relative camera position uncertainty of the bundle block adjustment result.

### Relative camera position and orientation uncertainties



	X[m]	Y[m]	Z[m]	Omega [degree]	Phi [degree]	Kappa [degree]
Mean	0.357	0.399	0.292	0.195	0.193	0.107
Sigma	0.461	0.533	0.358	0.244	0.228	0.145

### Manual Tie Points



MTP Name	Projection Error [pixel]	Verified/Marked
mp12	1.088	4 / 4
mp13	1.189	5 / 5
mp14	1.251	6 / 6
mp15	2.031	7 / 7
mp16	1.271	4 / 4
mp17	0.488	3 / 3
mp18	1.792	4 / 4

Projection errors for manual tie points. The last column counts the number of images where the manual tie point has been automatically verified vs. manually marked.

## Geolocation Details



### Ground Control Points



GCP Name	Accuracy XYZ [m]	Error X [m]	Error Y [m]	Error Z [m]	Projection Error [pixel]	Verified/Marked
Alter_Island (3D)	0.020/ 0.020	0.018	0.048	0.086	0.959	7 / 7
Breach2 (3D)	0.020/ 0.020	0.123	-0.116	10.895	1.938	3 / 3
Before_Breach (3D)	0.020/ 0.020	-0.157	-0.162	-0.201	1.261	7 / 7
Shed1 (3D)	0.020/ 0.020	-0.032	0.055	-0.001	0.738	16 / 16
Front_MainBuilding (3D)	0.020/ 0.020	0.096	-0.027	-0.128	0.638	7 / 7
Rice_Entrance (3D)	0.020/ 0.020	-0.040	0.044	-0.002	3.664	5 / 5
Mean [m]		0.001559	-0.026389	1.774741		
Sigma [m]		0.093309	0.085227	4.079743		
RMS Error [m]		0.093322	0.089219	4.449046		

0 out of 4 check points have been labeled as inaccurate.

Check Point Name	Accuracy XYZ [m]	Error X [m]	Error Y [m]	Error Z [m]	Projection Error [pixel]	Verified/Marked
Top_Arm		0.7134	0.3093	0.2500	0.3725	5 / 5
Island		-0.1301	0.1171	0.3341	0.5560	9 / 9
Side_MainBuilding		0.0759	0.0219	-0.3380	0.7100	7 / 7
Behind_MainBuilding		0.2332	-0.1166	-0.4880	0.7494	6 / 6
Mean [m]		0.223091	0.082960	-0.060458		
Sigma [m]		0.310991	0.154866	0.357713		
RMS Error [m]		0.382734	0.175687	0.362786		

Localisation accuracy per GCP and mean errors in the three coordinate directions. The last column counts the number of calibrated images where the GCP has been automatically verified vs. manually marked.

### Absolute Geolocation Variance



Mn Error [m]	Max Error [m]	Geolocation Error X [%]	Geolocation Error Y [%]	Geolocation Error Z [%]
-	-0.13	0.00	0.00	11.60
-0.13	-0.10	0.00	0.00	2.73

-0.10	-0.08	0.00	0.00	4.10
-0.08	-0.05	0.00	0.68	5.80
-0.05	-0.03	1.71	3.41	5.80
-0.03	0.00	53.24	47.44	24.57
0.00	0.03	43.69	45.39	21.50
0.03	0.05	1.02	2.39	8.87
0.05	0.08	0.34	0.68	5.80
0.08	0.10	0.00	0.00	1.02
0.10	0.13	0.00	0.00	2.39
0.13	-	0.00	0.00	5.80
Mean [m]		-0.144930	0.943150	-35.011505
Sigma [m]		0.009434	0.013447	0.131215
RMS Error [m]		0.145236	0.943245	35.011751

Min Error and Max Error represent geolocation error intervals between -1.5 and 1.5 times the maximum accuracy of all the images. Columns X, Y, Z show the percentage of images with geolocation errors within the predefined error intervals. The geolocation error is the difference between the initial and computed image positions. Note that the image geolocation errors do not correspond to the accuracy of the observed 3D points.

Geolocation Bias	X	Y	Z
Translation [m]	-0.144662	0.944101	-34.986790

Bias between image initial and computed geolocation given in output coordinate system.

## Relative Geolocation Variance



Relative Geolocation Error	Images X[%]	Images Y[%]	Images Z[%]
[-1.00, 1.00]	89.08	81.57	47.78
[-2.00, 2.00]	97.61	92.83	64.85
[-3.00, 3.00]	99.32	96.93	75.43
Mean of Geolocation Accuracy [m]	0.012918	0.012918	0.028515
Sigma of Geolocation Accuracy [m]	0.002439	0.002439	0.007267

Images X, Y, Z represent the percentage of images with a relative geolocation error in X, Y, Z.

Geolocation Orientational Variance	RMS [degree]
Omega	12.717
Phi	5.691
Kappa	7.349

Geolocation RMS error of the orientation angles given by the difference between the initial and computed image orientation angles.

## Initial Processing Details



### System Information



Hardware	CPU: Intel(R) Xeon(R) CPU E5-1620 v3 @ 3.50GHz RAM: 32GB GPU: NVIDIA Quadro K5200 (Driver: 21.21.13.6939), RDPDD Chained DD (Driver: unknown), RDP Encoder Mirror Driver (Driver: unknown), RDP Reflector Display Driver (Driver: unknown)
Operating System	Windows 7 Enterprise, 64-bit

### Coordinate Systems



Image Coordinate System	WGS84
Ground Control Point (GCP) Coordinate System	NAD83 / UTM zone 18N
Output Coordinate System	NAD83 / UTM zone 18N

## Processing Options



Detected Template	<input type="radio"/> 3D Maps
Keypoints Image Scale	Full, Image Scale: 1
Advanced: Matching Image Pairs	Aerial Grid or Corridor
Advanced: Matching Strategy	Use Geometrically Verified Matching: no
Advanced: Keypoint Extraction	Targeted Number of Keypoints: Automatic
Advanced: Calibration	Calibration Method: Standard Internal Parameters Optimization: All External Parameters Optimization: All Rematch: Auto, no

## Point Cloud Densification details



## Processing Options



Image Scale	multiscale, 1/2 (Half image size, Default)
Point Density	Optimal
Minimum Number of Matches	3
3D Textured Mesh Generation	yes
3D Textured Mesh Settings:	Resolution: Medium Resolution (default) Color Balancing: no
LOD	Generated: no
Advanced: 3D Textured Mesh Settings	Sample Density Divider: 1
Advanced: Image Groups	group 1
Advanced: Use Processing Area	yes
Advanced: Use Annotations	yes
Time for Point Cloud Densification	36m:08s
Time for Point Cloud Classification	NA
Time for 3D Textured Mesh Generation	09m:03s

## Results



Number of Generated Tiles	1
Number of 3D Densified Points	24897903
Average Density (per m <sup>3</sup> )	86.54

## DSM, Orthomosaic and Index Details



## Processing Options



DSM and Orthomosaic Resolution	1 x GSD (3.08 [cm/pixel])
DSM Filters	Noise Filtering: yes Surface Smoothing: yes, Type: Sharp
Raster DSM	Generated: yes Method: Inverse Distance Weighting Merge Tiles: yes
Orthomosaic	Generated: yes Merge Tiles: yes GeoTIFF Without Transparency: no Google Maps Tiles and KML: no
Time for DSM Generation	02h:25m:26s
Time for Orthomosaic Generation	01h:16m:26s
Time for DTM Generation	00s
Time for Contour Lines Generation	00s
Time for Reflectance Map Generation	00s
Time for Index Map Generation	00s

Low tide report without incorporated GCPs.

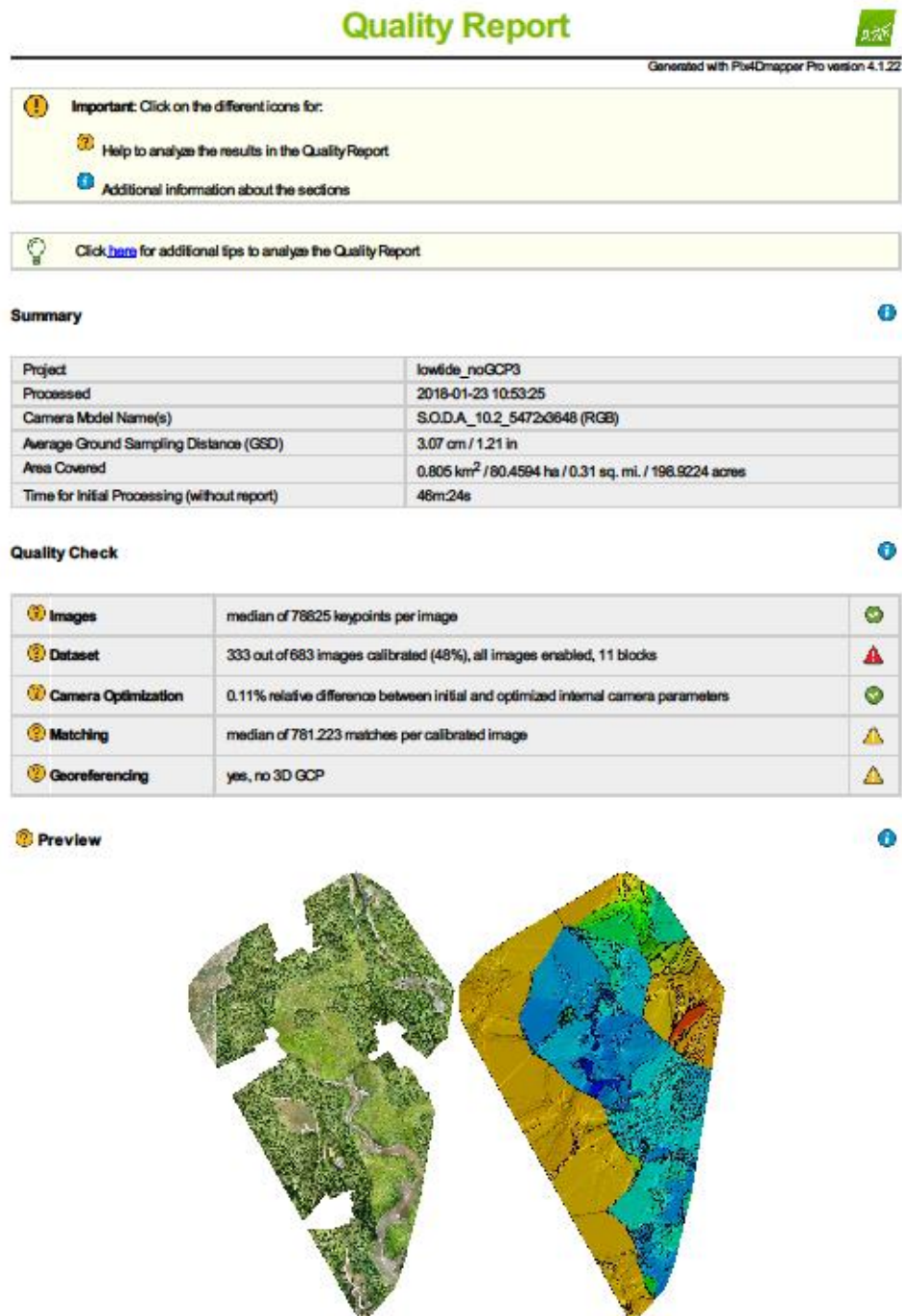


Figure 1: Orthomosaic and the corresponding sparse Digital Surface Model (DSM) before densification.

## Calibration Details



Number of Calibrated Images	333 out of 683
Number of Geolocated Images	683 out of 683

### Initial Image Positions

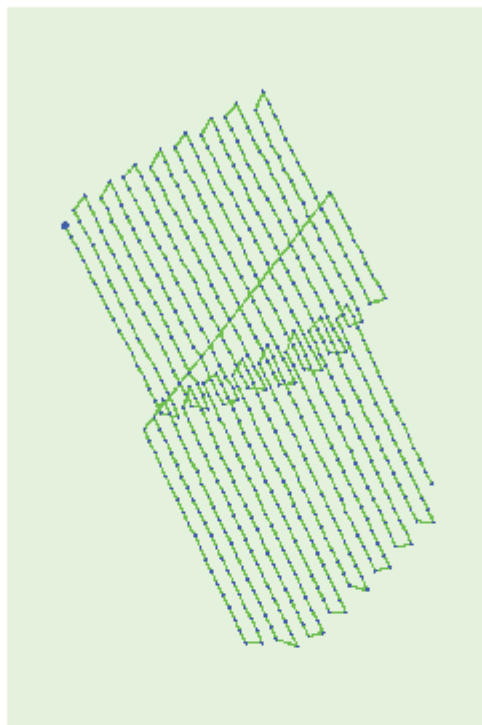


Figure 2: Top view of the initial image position. The green line follows the position of the images in time starting from the large blue dot.

### Computed Image/GCPs/Manual Tie Points Positions



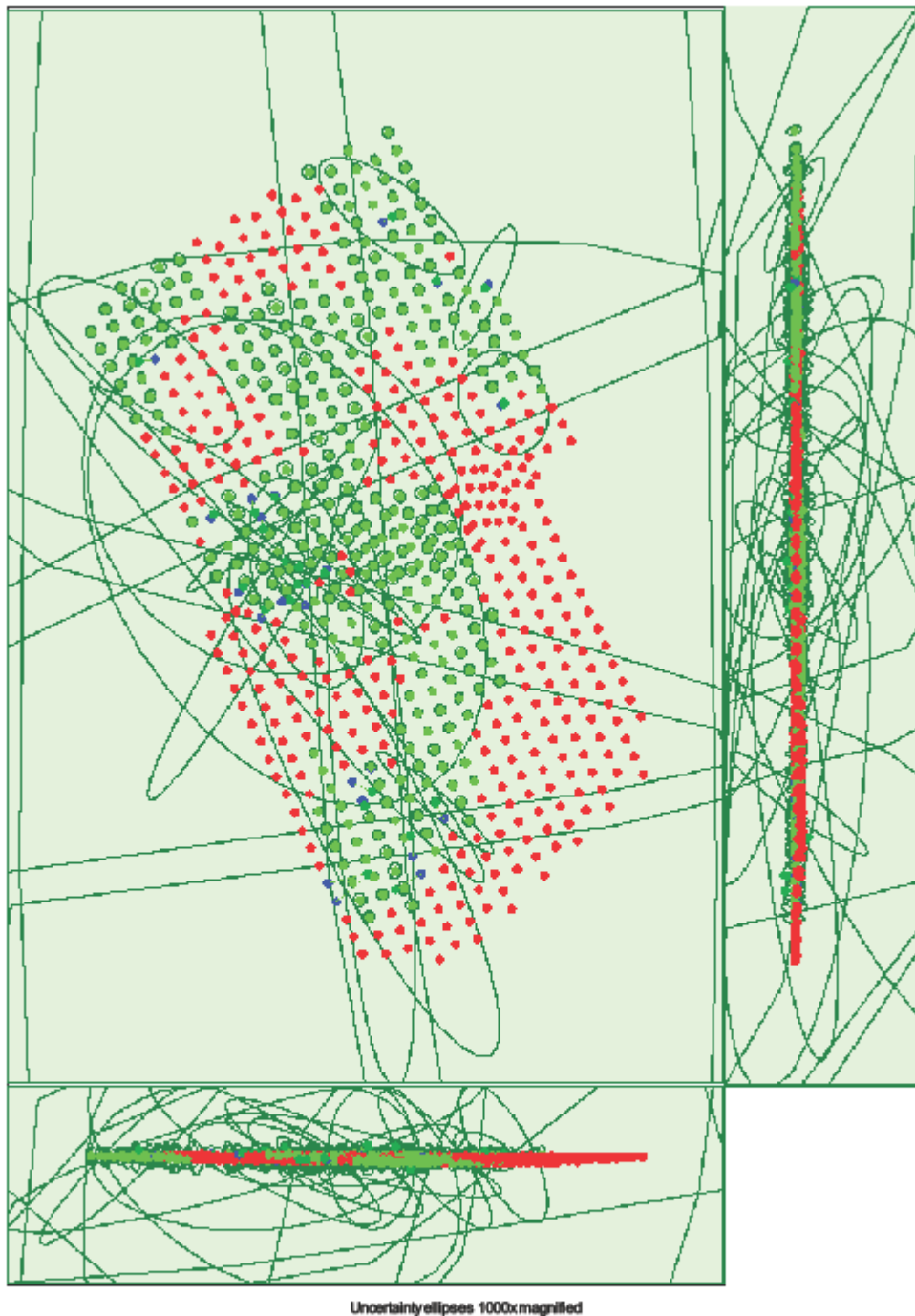


Figure 3: Offset between initial (blue dots) and computed (green dots) image positions as well as the offset between the GCPs initial positions (blue crosses) and their computed positions (green crosses) in the top-view (XY plane), front-view (XZ plane), and side-view (YZ plane). Red dots indicate disabled or uncalibrated images. Dark green ellipses indicate the absolute position uncertainty of the bundle block adjustment result.

	X[m]	Y[m]	Z[m]	Omega [degree]	Phi [degree]	Kappa [degree]
Mean	0.055	0.090	0.051	0.054	0.050	0.041
Sigma	0.264	0.604	0.188	0.262	0.238	0.178

#### 📷 Overlap

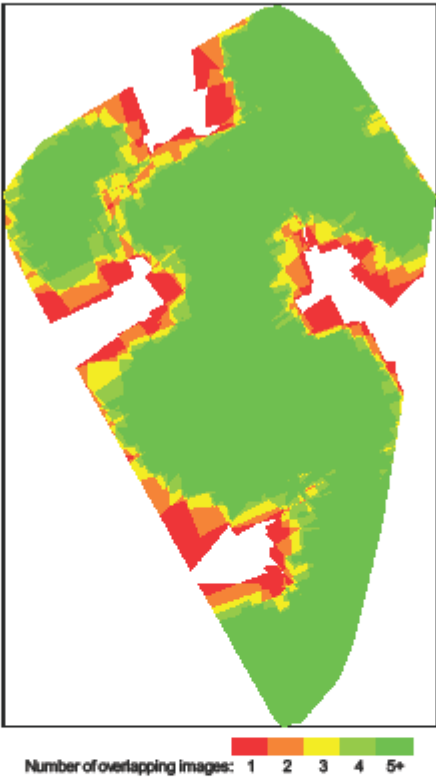


Figure 4: Number of overlapping images computed for each pixel of the orthomosaic. Red and yellow areas indicate low overlap for which poor results may be generated. Green areas indicate an overlap of over 5 images for every pixel. Good quality results will be generated as long as the number of keypoint matches is also sufficient for these areas (see Figure 5 for keypoint matches).

## Bundle Block Adjustment Details



Number of 2D Keypoint Observations for Bundle Block Adjustment	487345
Number of 3D Points for Bundle Block Adjustment	163225
Mean Reprojection Error [pixels]	0.153

#### 📷 Internal Camera Parameters

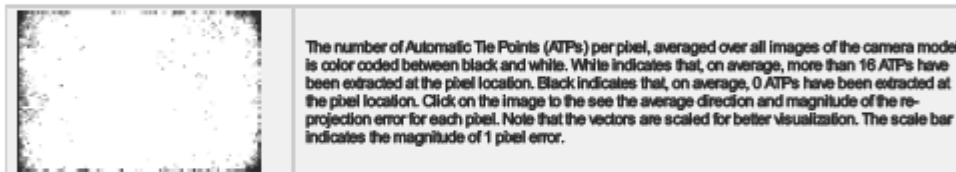
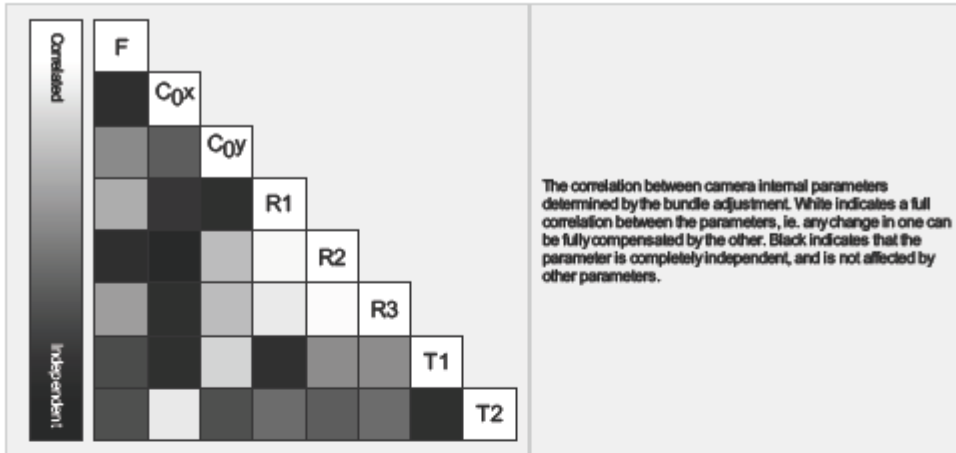
📷 S.O.D.A.\_10\_2\_5472x3648 (RGB). Sensor Dimensions: 13.132 [mm] x 8.755 [mm]



EXIF ID: S.O.D.A.\_10\_2\_5472x3648

	Focal Length	Principal Point x	Principal Point y	R1	R2	R3	T1	T2
Initial Values	4383.639 [pixel] 10.520 [mm]	2684.442 [pixel] 6.442 [mm]	1818.911 [pixel] 4.365 [mm]	-0.121	-0.192	0.262	-0.000	-0.002
Optimized Values	4378.769 [pixel] 10.508 [mm]	2745.418 [pixel] 6.588 [mm]	1777.074 [pixel] 4.265 [mm]	0.120	-0.425	0.390	-0.002	-0.000

Uncertainties (Sigma)	0.747 [pixel] 0.002 [mm]	0.382 [pixel] 0.001 [mm]	0.424 [pixel] 0.001 [mm]	0.001	0.002	0.003	0.000	0.000
-----------------------	-----------------------------	-----------------------------	-----------------------------	-------	-------	-------	-------	-------



## 2D Keypoints Table

	Number of 2D Keypoints per Image	Number of Matched 2D Keypoints per Image
Median	78825	781
Min	42545	38
Max	91262	12814
Mean	77006	1463

## 3D Points from 2D Keypoint Matches

	Number of 3D Points Observed
In 2 Images	140892
In 3 Images	29804
In 4 Images	11243
In 5 Images	5457
In 6 Images	2774
In 7 Images	1553
In 8 Images	885
In 9 Images	467
In 10 Images	238
In 11 Images	144
In 12 Images	92
In 13 Images	47
In 14 Images	23
In 15 Images	3
In 16 Images	3

## 2D Keypoint Matches

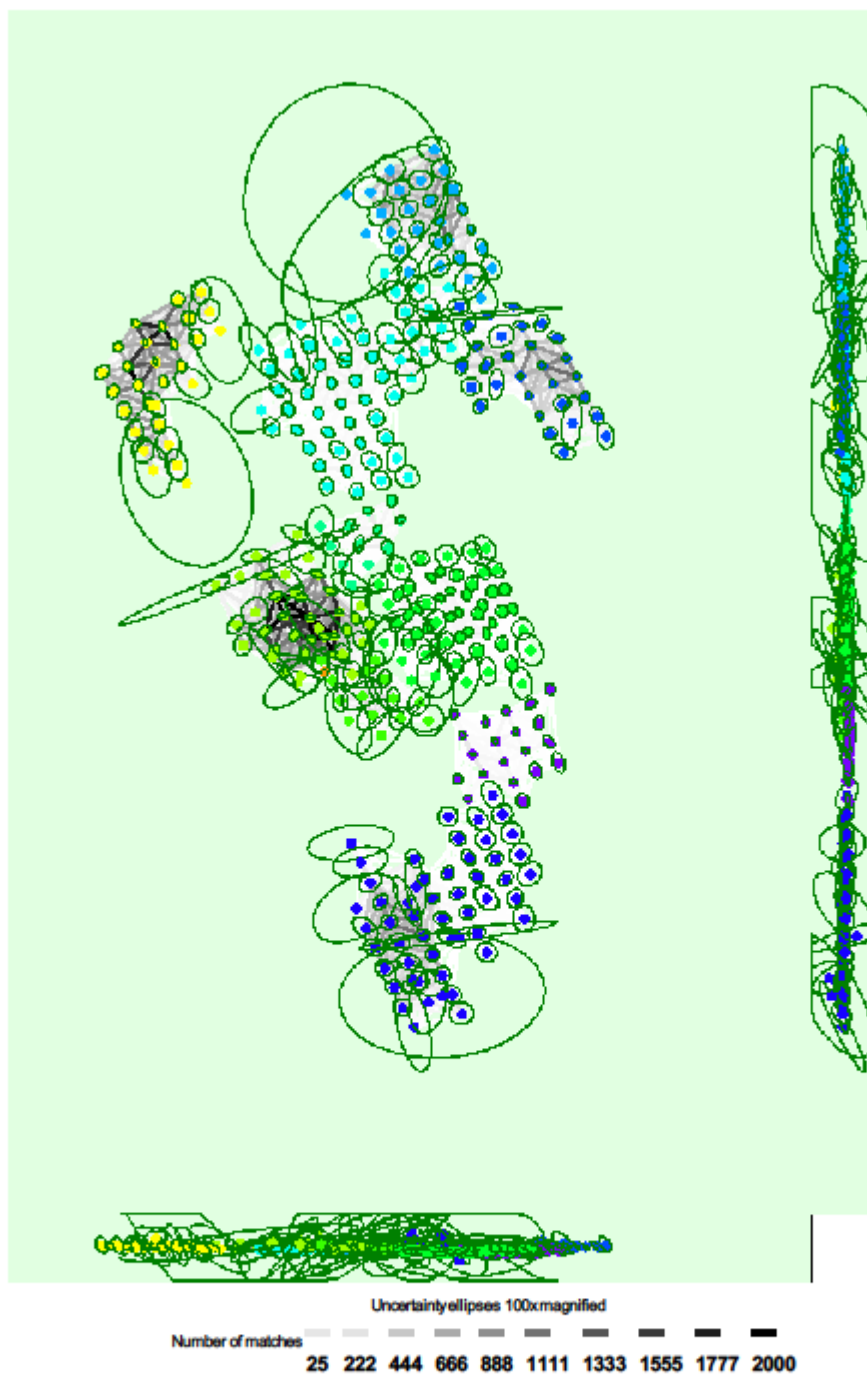


Figure 5: Computed image positions with links between matched images. The darkness of the links indicates the number of matched 2D keypoints between the images. Bright links indicate weak links and require manual tie points or more images. Dark green ellipses indicate the relative camera position uncertainty of the bundle block adjustment result.

#### Relative camera position and orientation uncertainties

X[m]	Y[m]	Z[m]	Omega [degree]	Phi [degree]	Kappa [degree]
------	------	------	----------------	--------------	----------------

Mean	0.221	0.218	0.134	0.109	0.100	0.065
Sigma	0.283	0.220	0.155	0.116	0.105	0.062

## Geolocation Details

### Ground Control Points

0 out of 4 check points have been labeled as inaccurate.

Check Point Name	Accuracy XYZ [m]	Error X [m]	Error Y [m]	Error Z [m]	Projection Error [pixel]	Verified/Marked
Top_Arm		0.383	0.096	0.633	0.308	4 / 4
Island		0.230	0.259	0.608	0.202	4 / 4
Side_MainBuilding		0.330	-0.466	-0.216	0.162	4 / 4
Behind_MainBuilding		0.481	-0.504	-0.322	0.309	3 / 3
Mean [m]		0.356003	-0.153887	0.175896		
Sigma [m]		0.090504	0.336679	0.446553		
RMS Error [m]		0.367327	0.370181	0.479947		

Localisation accuracy per GCP and mean errors in the three coordinate directions. The last column counts the number of calibrated images where the GCP has been automatically verified vs. manually marked.

### Absolute Geolocation Variance

Mn Error [m]	MaxError [m]	Geolocation Error X [%]	Geolocation Error Y [%]	Geolocation Error Z [%]
-	-0.13	0.00	0.00	9.71
-0.13	-0.10	0.00	0.00	0.00
-0.10	-0.08	0.00	0.00	1.62
-0.08	-0.05	0.00	1.29	1.29
-0.05	-0.03	1.29	2.59	5.18
-0.03	0.00	51.13	43.37	34.95
0.00	0.03	46.93	50.81	33.66
0.03	0.05	0.65	1.62	5.18
0.05	0.08	0.00	0.00	0.97
0.08	0.10	0.00	0.32	2.27
0.10	0.13	0.00	0.00	0.32
0.13	-	0.00	0.00	4.65
Mean [m]		-0.000367	-0.000603	-0.018730
Sigma [m]		0.007168	0.012485	0.120324
RMS Error [m]		0.007177	0.012500	0.121773

Min Error and Max Error represent geolocation error intervals between -1.5 and 1.5 times the maximum accuracy of all the images. Columns X, Y, Z show the percentage of images with geolocation errors within the predefined error intervals. The geolocation error is the difference between the initial and computed image positions. Note that the image geolocation errors do not correspond to the accuracy of the observed 3D points.

### Relative Geolocation Variance

Relative Geolocation Error	Images X [%]	Images Y [%]	Images Z [%]
[-1.00, 1.00]	92.56	89.32	70.55
[-2.00, 2.00]	98.71	94.82	80.91
[-3.00, 3.00]	100.00	96.76	82.52
Mean of Geolocation Accuracy [m]	0.012743	0.012743	0.027909
Sigma of Geolocation Accuracy [m]	0.002500	0.002500	0.007439

Images X, Y, Z represent the percentage of images with a relative geolocation error in X, Y, Z.

Geolocation Orientational Variance	RMS [degree]
Omega	5.353
Phi	4.371
Kappa	5.155

Geolocation RMS error of the orientation angles given by the difference between the initial and computed image orientation angles.

## Initial Processing Details

### System Information

Hardware	CPU: Intel(R) Xeon(R) CPU E5-1620 v3 @ 3.50GHz RAM: 32GB GPU: NVIDIA Quadro K5200 (Driver: 21.21.13.6939), RDPDD Chained DD (Driver: unknown), RDP Encoder Mirror Driver (Driver: unknown), RDP Reflector Display Driver (Driver: unknown)
Operating System	Windows 7 Enterprise, 64-bit

### Coordinate Systems

Image Coordinate System	WGS84
Output Coordinate System	WGS 84 / UTM zone 18N

### Processing Options

Detected Template	H 3D Maps
Keypoints Image Scale	Full, Image Scale: 1
Advanced: Matching Image Pairs	Aerial Grid or Corridor
Advanced: Matching Strategy	Use Geometrically Verified Matching: no
Advanced: Keypoint Extraction	Targeted Number of Keypoints: Automatic
Advanced: Calibration	Calibration Method: Standard Internal Parameters Optimization: All External Parameters Optimization: All Rematch: Auto, no